Last Glacial loess in Europe: luminescence database and chronology of deposition

Mathieu Bosq[1], Sebastian Kreutzer[2,3,4], Pascal Bertran[1,5], Philippe Lanos[4,6], Philippe Dufresne[4,6], Christoph Schmidt[7]

[1] PACEA, UMR 5199 CNRS - Université Bordeaux, allée Geoffroy Saint Hilaire, 33615 Pessac, France

[2] Institute of Geography, Ruprecht-Karl University of Heidelberg, Im Neuenheimer Feld 348, 69120 Heidelberg, Germany

[3] Geography & Earth Sciences, Aberystwyth University, Wales, United Kingdom

[4] Archéosciences-Bordeaux, UMR 6034, CNRS - Université Bordeaux Montaigne, Maison de l'Archéologie, 33607 Pessac, France

[5] Inrap, 140 avenue du Maréchal Leclerc, 33130 Bègles, France

[6] Géosciences-Rennes, UMR 6118 CNRS - Université de Rennes 1, 35042 Rennes, France

[7] Institute of Earth Surface Dynamics - University of Lausanne, Géopolis, 1015 Lausanne, Switzerland

Correspondence to: Mathieu Bosq (mathieu.bosq@gmail.com) and Sebastian Kreutzer (sebastian.kreutzer@uni-heidelberg.de)

Abstract. During the last glacial period, the climate shift to cold conditions associated with changes in atmospheric circulation and vegetation cover resulted in the development of large aeolian systems in Europe. On a regional scale, many factors may have influenced dust dynamics, such as the latitudinal difference between the various aeolian systems and the variability of the sources of wind-transported particles. Therefore, the assumption that the timing of aeolian deposition is strictly synchronous in Europe does not seem to be the most plausible hypothesis and needs to be evaluated. To test this assumption, the chronology of loess deposition in different European regions was investigated by studying 93 luminescence-dated loess-palaeosol sequences with their data recalculated and compiled in a single CSV file: the ChronoLoess database. Our study shows that the two major aeolian systems, the Northern European Loess Belt (NELB) on the one hand and the systems associated with the rivers draining the Alpine Ice Sheet on the other hand, developed asynchronously. The significant deposition started at about 32 ka b2k for the NELB vs 42 ka b2k for the perialpine loess and peaked about two millennia later for the former (21.8 ka b2k vs 23.9 ka b2k, respectively). This shift resulted mainly from the time lag between the maxima of the Alpine and Fennoscandian ice sheets, which acted as the primary sources of fine-grained particles through glacial abrasion. The major geomorphic changes that resulted from the development and decay of the Fennoscandian and British-Irish ice sheets also played an important role. Particularly, ice sheet coalescence during the LGM diverted meltwater fluxes through the Manche River and provided vast amounts of glacial particles available for deflation in the western NELB. The period during which the maximum Mass Accumulation Rate was reached for each loess-palaeosol sequence is relatively homogeneous in the NELB and ranges from 30 ka b2k to 19 ka b2k, whereas it is more scattered in the perialpine systems (>60 ka b2k to 14 ka b2k). This probably resulted from a combination of factors, including the asynchrony of maximum valley glacier advances and local geomorphic factors.

1 Introduction

During the Last Glacial, large aeolian systems developed in Europe in the periphery of the Fennoscandian (FIS) and Alpine (AIS) ice sheets and the rivers they fed, as well as along the Atlantic coast and in some intracontinental basins (Bertran et al., 2021; Lehmkuhl et al., 2021). In most cases, these aeolian systems each comprised a sand belt (sand sheets, dune fields) and a loess belt corresponding to the dust accumulation area at a greater distance from the particle sources. The formation of these aeolian systems was primarily controlled by a global climate shift towards cold conditions associated with changes in the regional atmospheric circulation over Europe relative to present-day conditions. During the Last Glacial Maximum (LGM), a

strong semi-permanent anticyclone over the FIS resulted in a significant increase in easterly winds instead of the currently prevailing westerly winds (Dietrich and Seelos, 2010; Ludwig et al., 2016; Schaffernicht et al., 2020), which intensified the cooling of Europe and the southward extension of permafrost (Stadelmaier et al., 2021). The altered atmospheric circulation

45 also promoted an increase in the frequency and intensity of storms over Central Europe and the Mediterranean regions due to a stronger, southwardly shifted jet stream (Löfverström et al., 2014; Beghin et al., 2015; Luetscher et al., 2015; Ludwig et al., 2016; Pinto and Ludwig, 2020; Kageyama et al., 2021). These climatic changes were particularly favourable to intensive aeolian dynamics in a context where precipitation was substantially lower, and vegetation cover was less dense and wooded than today. Continental-scale climate control is the main explanation behind the widespread Last Glacial deposition of aeolian

50 sediments in Europe (Rousseau et al., 2007, 2017, 2021; Antoine et al., 2009).

However, on a regional scale, many factors modulated aeolian activity. These factors are linked to the latitudinal difference between the various aeolian systems and the variability of the sources of wind-transported particles. As already suggested by some authors based on arguments of loess distribution and thickness (e.g., Smalley and Leach, 1978; Bertran et al., 2021), glacial abrasion at the base of ice sheets (FIS, British-Irish ice sheet (BIIS), AIS) was the primary provider of the "rock flour"

55 (e.g., Summerfield, 2014), the fine-grained particles in LGM Europe, which were then transported by rivers and made available to deflation in floodplains. This agrees with studies in modern cold environments, which show that aeolian sedimentation is usually closely associated with glaciofluvial systems (Dijkmans and Törnqvist, 1991; Hugenholtz and Wolfe, 2010; Bullard, 2013; Arnalds et al., 2016; Bullard and Mockford, 2018). Recent advances in moraine dating have revealed asynchronous growth and recession of the European ice sheets due to changing moisture sources and atmospheric circulation (Luetscher et

60 al., 2015; Monegato et al., 2017). In addition, deglaciation (especially of the FIS) was associated with major palaeogeographic changes, with a complete reorganisation of the drainage network during the rapid retreat of the ice sheet (Patton et al., 2017). Therefore, the availability and source areas of wind-blown particles must have changed over time and in different ways depending on the regions considered. For Atlantic coastal systems and intracontinental basins, particles were not of glacial origin but derived from other sources (frost weathering of rocks, soil erosion by deflation, aeolian abrasion, fluvial

65 comminution). The controlling factors are likely to have been significantly different from those that drove glacial fluctuations. Among other factors, the impact of permafrost and vegetation changes has been mentioned by some authors (Kasse, 1997; Sitzia et al., 2017; Bosq et al., 2018). Therefore, the assumption that the timing of aeolian deposition is strictly synchronous in Europe does not seem to be the most plausible hypothesis and needs to be evaluated through detailed chronological studies of loess-palaeosol sequences (LPS) from different European regions using a large dataset.

70 To test this assumption, the present study reviews the chronology of loess deposition between 60 ka to the present based on a compilation of recently published luminescence data, i.e., optically stimulated Luminescence (OSL, Huntley et al., 1985) on quartz grains and infrared stimulated luminescence (IRSL, Hütt et al., 1988 and post-IR IRSL, Thomsen et al., 2008) on feldspars and polymineral fine grains. Despite the relatively significant uncertainties of luminescence ages (e.g., INQUA Dune Atlas luminescence ages, v2021-11, Lancaster et al., 2015: relative age uncertainty varies from 7% (Q_{1st}) to 12% (Q_{3rd}), n =

75 5687), we have chosen the chronological data from these methods because of the high number of well-dated LPS and their pan-European spatial distribution. Recent studies have shown that terrestrial gastropod shells and earthworm calcite granules can be used to obtain a precise loess chronology (Újvári et al., 2016, 2017; Moine et al., 2017, 2021). While these carbonates are relatively abundant in loess deposits, unfortunately, radiocarbon-based chronologies remain scarce. Furthermore, they cannot be used with confidence for dating loess deposits in southern Europe because of strong syn-sedimentary bioturbation

80 and reworking processes (e.g., Bosq et al., 2020).

All published luminescence ages used here were recalculated based on published information, taking into consideration several parameters (such as equivalent doses, radionuclide concentration, *etc*.), and the chronological distribution of the resulting ages was analysed. Bayesian-based age-depth models were then calculated for a restricted number of available LPS from each study region. From these age-depth models, Mass Accumulation Rates (MARs) (Kohfeld and Harrison, 2003) were estimated and

85 discussed in relation to regional palaeoclimatic records. All recalculated data used for this study are provided under Creative Comments (CC-BY) licence conditions for future studies (ChronoLoess database, v1.0.0; Bosq et al., 2023).

2 Methods

2.1 Chronological data

2.1.1 ChronoLoess database

90 In the present study, we have collected luminescence ages from 77 publications in a database called "ChronoLoess database", including 93 LPS from 16 European loess regions (**Fig. 1**). The data were selected according to the following two criteria: (1) only papers published after the year 2000 were used and (2) only loess deposits accumulated during the Last Glacial were considered. In 2000, the single-aliquot regenerative-dose (SAR) protocol for OSL (Murray and Wintle, 2000) on quartz and IRSL measurements on feldspar (Wallinga et al., 2000) was introduced. In conjunction with the advent of automatised

95 instruments (e.g., Bøtter-Jensen et al., 1999; Duller et al., 1999a, 1999b), those developments mark not only significant stepstones on the way to the success of luminescence-dating in Quaternary sciences, but the following homogenisation of protocols and measurements equipment also make luminescence ages better comparable.

A total of 1,423 luminescence ages from quartz, feldspar or polymineral fractions were used. We did not use published ages, but we manually extracted numerical parameters from the original papers such as radionuclide concentrations or equivalent

100 doses, compiled them in *MS Excel^{TM}*, and recalculated the ages with the dose rate and age calculator *DRAC* (v.1.2, Durcan et al., 2015) (see Sec. 2.1.2 for more details).

We provide this database in version 1.0.0 as XLS and CSV files via Zenodo (Bosq et al., 2023) to make it available to the scientific community. This database is meant to receive rolling updates in future, including more recent age data.

2.1.2 Recalculating published luminescence ages

105 While some isolated recommendations exist for reporting luminescence data (e.g., Duller, 2008; Bateman, 2019; DKE/K 967, 2022; Mahan et al., 2022), those are seldom followed. Similarly, software tools used to analyse data and calculate ages often remain unreported (for a discussion, see Kreutzer et al., 2017). This situation puts up a barrier that severely impedes the recycling and comparison of luminescence age records and is further complicated by the number of single parameters to consider for age calculation. Unfortunately, there is no simple way to circumnavigate this issue and tap into the otherwise

110 excellent and unique chronological datasets covering mainly the Late Pleistocene. In order to use the published luminescence data in our chronological modelling, we made a couple of processing decisions as outlined in the following.

1. As mentioned in Sec. 2.1.1, we did not use published ages but extracted numerical quantities published along the ages, such as radionuclide concentrations. This decision allowed us to cancel out systematic deviations between datasets resulting from, e.g., age calculation software tools and applied dose-rate conversion factors.

115 2. We treated most datasets reporting infrared-stimulated luminescence (IRSL, including IRSL data after different thermal treatments, so-called post-IR IRSL data) as minimum ages to avoid incorporating potential systematic errors from fading corrections (cf. King et al., 2018) and measurements of the fading rate itself. Higher signal stability was reported for ages derived from post-IR IRSL at 290 ˚C measurements (e.g., Buylaert et al., 2012), and studies often assumed negligible fading or reported inconclusive results that allowed the authors to circumvent a fading correction.

120 Residual doses, as far as reported, were not subtracted (we refer the reader to the database for details on selected and discarded datasets).

3. We recalculated all cosmic and environmental dose rates using *DRAC* (v.1.2, Durcan et al., 2015). The external Rb concentration was always calculated from K. This decision bears the risk that the Rb concentration might not best reflect the true Rb concentration in all cases (cf. Mejdahl, 1987; Huntley and Hancock, 2001; Buylaert et al., 2018).

However, we decided to follow Mejdahl's conclusion that in absent of measured Rb values, which was the case for all studies except for Fenn et al. (2020), a calculation of Rb from K is still better than not having taken Rb into account.

In rare cases, the original study did not report sufficient information but provided only processed data for, e.g., cosmic and environmental dose rates, and the data could not be recalculated.

4. Except for rare cases of apparent mistakes (for instance, typos), other parameters combined with high degrees of freedom (e.g., alpha-efficiency, internal dose rates, measurement protocol parameters, statistical data treatment) were always taken as reported by the study's authors. Missing or faulty units and citations (e.g., obviously unsuitable reference) were not considered errors if these data appeared meaningful otherwise.

5. The final age uncertainties do not include systematic uncertainties, except those already part of tabulated values.

In other words, we placed wagers on the authors' knowledge and insight, making expert decisions on individual parameters, which includes fundamental decisions such as the chosen mineral and grain size fraction or the method to estimate radionuclide concentrations. Suppose an original study (including the supplement) did not provide sufficient information to recalculate the luminescence ages in sporadic cases. Such results were considered non-reproducible and discarded. For the list of parameter selections, we refer to **Table S1** in the supplement.

Our selection remains imperfect without accessing and re-analysing primary data (e.g., BIN/BINX files containing luminescence measurements). However, such data are usually unavailable without contacting study authors on a case-to-case basis. Still, the amount of pooled data likely leads to averaging effects in the case of extreme values, providing sufficient statistical confidence in the modelling results. In the following, all ages are reported in ka before 2000 (b2k).

2.1.3 Calculation of time-activity curves

In our results, we will present time-activity curves. The time-activity curve characterises the rate of events over time. It gives the number of events (here, the number of dated dust accumulation events) that have occurred per unit of time. It is also called the cumulative probability density function (CPDF) because it is equal to the probability density (or probability distribution) of events over time multiplied by the total number of dates n. Different approaches to estimating this activity curve have been proposed and discussed in the literature, mainly based on the histogram method (Vermeesch, 2012) or density estimation by kernel methods (Vermeesch, 2012; Contreras and Meadows, 2014; Bronk Ramsey, 2017). However, these methods do not take into account errors on dates and do not allow the calculation of an error envelope on the estimated density. This is why we propose to estimate this density by the sliding window method, which uses a uniform kernel of width h (Rivoirard and Stoltz, 2012; Lanos and Dufresne, 2022). In this case, the number of events that occur in a window of width h centred on a time θ is a random variable denoted $A(\theta, h)$ that follows a binomial distribution of n parameters (the total number of dated events) and $q(\theta)$ which represents the theoretical proportion of events that occur in the considered window. From this binomial probability law, we can deduce the average activity or expectation (here noted $E[.]$) of the number of events per unit of time, i.e.:

$$E[A(\theta, h)] = n \frac{q(\theta)}{h}$$

The parameter $q(\theta)$ is unknown: it is then estimated from the observed frequency $f_n(\theta)$, which is equal to the number n_i of dates observed in the window of width h centred on θ, divided by the total number of dates n. Since each date is affected by an uncertainty represented by a probability density, the contribution of a date to a given window will therefore be given by the probability that the date appears in the window interval. This value is between 0 (the date is not in the window) and 1 (the whole date distribution is in the window). This probability can be easily obtained by a large number of Monte Carlo draws in from the date distribution. Ultimately, the observed frequency for the window of width h centred on θ will be given by the sum of the probabilities of the dates belonging to the window divided by the total number of dates. Because of the binomial

distribution and from the observed frequency $f_n(\theta)$, it is possible to estimate the parameter $q(\theta)$ by an interval $q_1(\theta)$ and $q_2(\theta)$ at a 95% confidence level. This interval is obtained using the Clopper and Pearson (1934) chart. The 95% confidence interval (or error envelope) on the activity curve is derived by:

$$n\frac{q_1(\theta)}{h} \leq A(\theta, h) \leq n\frac{q_2(\theta)}{h}$$

170

The average activity $E[A(\theta, h)]$ is estimated by the expression: $n\frac{f_n(\theta)}{h}$

It is important to note that this is a point confidence interval, i.e. estimated at each point θ independently of the other points, and not a confidence band, i.e. of uniformity in θ (Rivoirard and Stoltz, 2012).

2.1.4 Comparison of the observed activity curve with the assumption of a uniform random distribution of dates

175   The question may arise whether the peaks or troughs observed on the activity curve are statistically significant for the assumption of a uniform random distribution of dates in the period considered. In the case where all dates are uniformly distributed between dates θ_m and θ_M, the date probability density becomes $q(\theta) = \frac{h}{(\theta_M - \theta_m)}$. This is represented by a rectangular graph of width $(\theta_M - \theta_m)$ and height $q(\theta)$. If this uniform distribution lies within the envelope of the 95% activity curve, this means that the peaks or troughs of the curve may not be significant, i.e., they may be the result of a uniform random

180   distribution of dates.

Another aspect point to discuss is the choice of the width h of the window. Given the geological problem posed, the idea here is to vary the width h to maximise the gap between the two curves, accounting for the error envelope. If a peak or trough, with its 95% error envelope, does not contain the uniform distribution, we can calculate a deviation which, summed over all the dates θ according to a fine exploration step, defines a global significance score S_h as a function of h. This score is analogous

185   to a distance in total variation between two probability distributions (Rivoirard and Stoltz, 2012), but here we take into account the 95% error envelope. The calculation of the activity curve is implemented in the chronological modelling application *ChronoModel* v2.0 (Lanos and Philippe, 2017a, b; Lanos and Dufresne, 2019), and the new *ChronoModel* v3.0 (Lanos and Dufresne, 2022) allows calculating the S_h score as a function of h. The width h that maximises this score is sought. The width h thus determined indicates the resolution on the date θ of a peak or trough, which does not contain the uniform distribution in

190   its envelope. The idea of maximising the S_h score emanates from the geological problem posed: we want to know if dated events are more frequent at certain periods than at others. We, therefore, search for the window width h that best highlights this deviation from date uniformity. Note that using a uniform kernel of width h (sliding window) necessarily produces an edge effect at the data's extremities (θ_m, θ_M). This is why we replace the rectangular distribution by a "trapezoid" distribution to correct this effect and allow comparison (the calculation of the significance score) with the activity curve.

195   ## 2.2 Bayesian age-depth modelling

2.2.1 Data selection

Bayesian age-depth modelling was performed on a limited number of LPS (n = 23) (see **Table 1**). The chronological models take into account both the recalculated luminescence ages (extracted from the ChronoLoess database) and Accelerator Mass Spectrometry (AMS) radiocarbon ages when available (see **Fig. S2**). Only LPS with more than 6 luminescence and/or

200   radiocarbon ages were retained. The published AMS radiocarbon ages were obtained from various materials, including charcoal fragments, gastropod shells and calcitic earthworm granules. Conventional radiocarbon ages were calibrated to calendar ages with the IntCal20 calibration curve (Reimer et al., 2020) using *ChronoModel* v3.0 (Lanos and Dufresne, 2022).

2.2.2 Overview of the method used in *ChronoModel*

The estimate of MARs is based on the building of age/depth curves. For this purpose, we used a Bayesian approach developed by P. Lanos in the *RenCurve* (Lanos, 2004); now implemented in the new version of *ChronoModel* v3.0 (Lanos and Dufresne, 2022). The Bayesian approach makes it possible to estimate a mean age-depth curve with its confidence envelope that interpolates the data and takes into account the uncertainties coming from the chronometric dates and errors in depth measurements (mostly small). Additional individual errors (so-called irreducible errors) are respectively added on the dates and depths to take into account the possible presence of outlying dates and stratigraphic inversions. This Bayesian modelling, therefore, automatically penalizes the influence of outliers. The curve estimation itself is based on penalized cubic spline function, which aims to realize a compromise between smoothing and fitting at the data points (age/depth), thanks to a smoothing parameter estimated using Bayesian modelling. It is important to note that the cubic spline works similarly to a kernel method where the bandwidth is thinner, the greater the point density over time (Green and Silverman, 1993). In other words, the smoothing adapts locally to the point density. The numerical calculation is carried out using MCMC techniques (Metropolis-Hastings algorithm) (Gilks et al., 1995) implemented in *ChronoModel*. For each age-depth sequence, 300 000 iterations were needed to obtain a precise estimation of the mean curve, its error envelope, the posterior irreducible variances (on time and depth) and the smoothing parameter. From the obtained age-depth curve we can estimate the rate of loess accumulation, which is given by the first derivative of the mean curve at each time.

An example of an age-depth curve is shown in **Fig. 2** (Balta Alba Kurgan), where dates have been determined by [14]C (green squares) and luminescence dating (red dots). Each point (square or dot) corresponds to the middle of the date interval at 95%, represented by a horizontal bar. Some depths are dated several times by ^{14}C and/or luminescence. The date intervals can therefore overlap for the same depth. We note in this example that some of the luminescence dates at the bottom are considered outliers and penalized during the mean curve calculation. This explains why the error envelope on the depth is more significant in this part.

2.2.3 Mass Accumulation Rates (MARs)

Reconstructing MARs is essential for a reliable picture of past dust deposition and comparison of loess records from different regions and for understanding and estimating past atmospheric mineral dust activity (Albani et al., 2015). This work requires independent and accurate high-resolution age-depth models. Therefore, based on the Bayesian age-depth models performed as part of this study (see the previous paragraph), we calculated the MARs for each LPS using the following equation proposed by Kohfeld and Harrison (2003):

$$MAR\ (g\ m^{-2}\ a^{-1}) = AR \times f_{eol} \times \rho_{dry}$$

where AR is the bulk accumulation rate (m.a[-1]), f_{eol} is the sediment fraction aeolian in origin (we assumed here to be 1), and ρ_{dry} is the bulk density of dry sediment (g.m^{-3}). Estimated bulk density values for loess vary in the literature and between loess regions (Frechen et al., 2003; Kohfeld and Harrison, 2003; Újvári et al., 2010). Here, we adapted a bulk density value of 1.5 g.cm^{-3} for our calculations based on the average loess values from the European region (Újvári et al., 2017; Perić et al., 2019; Fenn et al., 2020). For each LPS, mean MARs were calculated from the following formula:

$$MAR\ (g\ m^{-2}\ a^{-1}) = \left(\frac{depth_2 - depth_1}{age_2 - age_1}\right) \times f_{eol} \times \rho_{dry}$$

where *depth₁* and *depth₂* are the depths of the highest and lowest dated samples in the loess profile, respectively, and *age₁* and *age₂* are the modelled ages for the corresponding depths. This calculation avoids the high uncertainties associated with the ends of each age-depth model.

The dating resolution has an impact on the calculated MARs. This is particularly true for extreme MARS, i.e., the highest values for a given sequence. Long intervals between dates necessarily result in averaging MARs over the considered period. In this study, the chronological models consider the recalculated luminescence ages (extracted from the ChronoLoess database)

and AMS ^{14}C ages where available. Since many dates are available for the periods of greatest dust accumulation in most sequences, for example, nine levels have been dated for the Balta Alba Kurgan LPS between 35 ka b2k and 24 ka b2k and up to 13 levels for the Biały Kościół LPS between 28 ka b2k and 20 ka b2k. We consider the extreme MAR values obtained representative, although we acknowledge that we cannot exclude their exact timing might partly suffer from a dating resolution-related inaccuracy.

3 Results

3.1 ChronoLoess database: first results

In this study, we started with 1,423 recalculated luminescence ages. The quality of the data was estimated from the comparison of the ages reported in the original studies and the ages recalculated using *DRAC*. We considered age discrepancies of less than 10% acceptable, while larger discrepancies were considered errors requiring additional inspection or correction. As quality control, we randomly sampled 100 ages, which yielded reasonable age differences between 0.2% and 20% (see Supplementary Information for more details and **Fig. S1**). Some ages ($n = 7$) showed a discrepancy of >20%, which usually indicated input errors in the *DRAC* table, such as missing information or wrong input dimensions. We corrected those errors (which were then usually found in other datasets) and now assume that >95% of the data in the dataset are free of copy errors. In some cases, it turned out that the original study (and supplements) did not contain enough information to recalculate the ages. Thus, 247 ages were not included and were considered incorrect, non-reproducible or repetitions (typically if different luminescence protocols were tested in a study). In addition, we focused only on a study period ranging from 60 ka b2k to the present, eliminating 205 additional ages. Nevertheless, some of these older ages were used in the generation of age-depth models (see Sec. 3.2). This selection finally left us with 971 ages extracted from the database available for the analysis of loess deposition.

The ages obtained are unevenly distributed in 16 loess regions: Southern England ($n = 20$); Northern France / Belgium ($n = 42$); Saxony (Germany) ($n = 55$); Southern Poland ($n = 134$); Upper Rhine (upstream of Mainz) ($n = 46$); Middle Rhine Valley/Lower Rhine Embayment (Middle/Lower Rhine) ($n = 101$); Harz (Germany) ($n = 19$); Upper Danube ($n = 75$); Carpathian basin (Middle Danube) ($n = 188$); Lower Danube ($n = 143$); Dniester ($n = 21$); Prut ($n = 18$); Moravia ($n = 20$); Po ($n = 47$); Rhone ($n = 19$); Ebro/Tajo ($n = 23$). In regions where the number of ages selected is greater than 100 (e.g., Carpathian basin, Middle Rhine Valley/Lower Rhine Embayment, Poland), representativeness is assumed to be acceptable. Results from other regions ($n \leq 100$) should be considered cautiously. These regions account for the majority of our dataset. Therefore, the recalculated ages were grouped into two sets corresponding to the main European loess regions, the Northern European Loess Belt (NELB) ($n = 371$) and the Perialpine Loess (PL) ($n = 517$) (see **Fig. 1** for the approximate boundary). Such a grouping avoids statistical under-representation for some regions and minimises the importance of local peculiarities, particularly the problems related to erosional phases in the LPS. Data from continental aeolian deposits disconnected from the main ice sheets, such as the Dniester, Prut, Tajo and Ebro basins and Moravia region, were excluded from our compilation due to the low number of ages available. As mentioned above, these aeolian systems are likely to provide a record different from the NELB and PL (e.g., Wolf et al., 2018) and would deserve to be dated more widely.

The two large groups correspond to distinct and relatively homogeneous aeolian systems. The NELB is a band of loess that developed south of the European Sand Belt (ESB, Zeeberg, 1998). It stretches in low relief areas between latitudes 48°N and 51°N approximately, from the tip of Brittany to the east of Poland (**Fig. 1**). The grain size distribution shows a gradual transition from coversands to sandy loess and loess (Bertran et al., 2021; Lehmkuhl et al., 2021). This grain size gradient is controlled by the distance to the glaciofluvial sources and topography in a context of low and sparse vegetation (tundra-steppe). This pattern and the chemical composition of loess, which is rich in potassic minerals and relatively poor in carbonates (Bosq et al., 2020b; Skurzyński et al., 2020), i.e. close to the composition of the felsic rocks of the Scandinavian Shield, suggest a common

285 supply predominantly from the outwash plains of the FIS. Mixing with local sources also influenced the chemical and mineralogical composition, explaining minor regional differences (Baykal et al., 2021). PL accumulated, often with marked asymmetry, along large rivers fed by the AIS (Danube, Po, Rhone, Rhine) (**Fig. 1**) and is characterised by a relatively homogeneous chemical composition, with a high carbonate content due to the abundance of calcareous rocks in the bedrock of the AIS (Buggle et al., 2008; Újvári et al., 2008; Bosq et al., 2020b). The coarse texture, poor grain size gradient and more

290 variable thickness make it distinct from North European loess. It has been suggested that capturing particles transported by saltation and short-term suspension by dense, shrubby vegetation typical of southern areas was the main factor in the dominant accumulation of coarse loess close to fluvial sources (Bosq et al., 2018; Bertran et al., 2021).

The age distribution of loess in these two areas is used here to indicate the aeolian dynamics over the last 60 millennia. It is represented by the activity curve and its 95% confidence interval (**Fig. 3**). Maximum age densities (i.e., clusters) with its

295 confidence envelope are shown as peaks exceeding the line representative of a uniform random distribution. These density maxima provide a chronological estimate of the main periods of dust accumulation. The bandwidth chosen in the following discussion was calculated to maximize the significance score, i.e., 8.1 ka for the NELB and 9.7 ka for PL.

At the continental scale, the comparison between the two areas highlights the following points (**Fig. 3**):

(1) The age distribution is not uniform over time, and clusters are clearly identifiable. These clusters reflect episodes of intense
300 aeolian accumulation and cover a time interval encompassing the Upper Pleniglacial, which coincides with the maximum advance of European glaciers (**Fig. 3A**). For older periods and the early Holocene, the age density is low and lies below the uniform distribution line. This indicates little to no aeolian sedimentation.

(2) Substantial loess deposition in the NELB started several millennia later than in the perialpine aeolian systems. In the former area, dust accumulation increased from about 32 ka b2k, i.e. from GS-5.2 (Rasmussen et al., 2014) and rose steeply
305 after 30 ka b2k, i.e. during GS-5.1 (**Fig. 3B**). In contrast, deposition in the perialpine area started earlier and increased as early as 42 ka b2k (GS-11), with a further rise after 40 ka b2k (GS-9) (**Fig. 3C**). Although the chronological limits of Heinrich Events (HEs) remain relatively imprecise, GS-5.1 and GS-9 correlate with HE-3 and HE-4 respectively in marine records (Sanchez Goñi and Harrison, 2010).

(3) For the PL, deposition peaked at 23.9 ka b2k (**Fig. 3B**), i.e., at the very end of GS-3 (HE-2). The age distribution in the
310 NELB contrasts with that of the perialpine loess. Dust accumulation peaked during the LGM at 21.8 ka b2k (GS-2.1c), then decreased sharply at the end of GS-2.1 (**Fig. 3C**). For both aeolian systems, the large bandwidth chosen, together with the uncertainty associated with the luminescence ages and the variability related to local factors do not allow for the identification of well-defined secondary peaks within the main accumulation period.

(4) When splitting the NELB data into two subsets, the eastern part (here referred to E-NELB, i.e., Poland, East Germany, *n*
315 = 208) and the western part (W-NELB, France, England, Belgium, West Germany, *n* = 163) shows contrasting activity curves. W-NELB shows a plateau between 26.5 ka b2k and 20.5 ka b2k, while E-NELB has a bell shape centred at 21.7 ka b2k (**Fig. 4**). Loess deposition thus appears to have started significantly earlier in the BIIS-influenced part of the NELB, and the peak accumulation lasted longer.

3.2 Mass Accumulation Rates

320 The spatial distribution of the LPS used to build the Bayesian age-depth models is shown in **Fig. 1**, while the sites studied are listed in **Table 1**. The chronological models take into account both the recalculated luminescence ages (extracted from the ChronoLoess database) and AMS ^{14}C ages when available. The distribution of sites does not appear spatially homogeneous, with notably a lack of well-dated LPS in the western part of the NELB (North France, Belgium) and a deficit in the Po Plain and the Upper Danube. These differences do not correspond to a field reality (lack of available sections) but reflect the current

325 state of research. Nevertheless, while awaiting further dating work, the number of age-depth models produced in this study (*n* = 23) allows for discussion of sediment accumulation rates at a pan-European scale.

During the study period (60 - 0 ka b2k), the mean sedimentation rates derived from Bayesian age-depth models vary between 0.05 mm.a^{-1} and 1.45 mm.a^{-1}, while the mean MARs range from 77 g.m^{-2}.a^{-1} to 2,181 g.m^{-2}.a^{-1}, with extreme MAR values of 150 g.m^{-2}.a^{-1} and 4,993 g.m^{-2}.a^{-1} (**Table 1**). **Fig. 5** shows a large variability of MARs between regions but also between sites within the same region, with MARs varying by an order of magnitude. We found the highest dust accumulation rates in Poland, in the Po and Rhine valleys, and observed the lowest fluxes in England and the Lower Danube. MARs also varied strongly over time (**Fig. 5**; **Fig. S3**). Age models based on radiocarbon dating show multiple peaks (e.g., Dunaszekcső, Madaras Nussloch) and better resolution compared to models using luminescence ages, which tend to smooth the curves (**Fig. S2**).

4 Discussion

4.1 Impact of ice sheets on aeolian dynamics

As previously demonstrated in many studies and despite chronological uncertainties, the bulk of loess accumulation occurred during MIS 2 (Antoine et al., 2009; Stevens et al., 2011; Guérin et al., 2017; Újvári et al., 2017; Zens et al., 2018; Moska et al., 2019b; Stevens et al., 2020; Perić et al., 2022). Our results unambiguously indicate that the main phase of accumulation occurred later for the NELB than for the PL. This phase started at about 32 ka b2k for the NELB vs 42 ka b2k for PL and peaked about two millennia later for the former (21.8 ka b2k vs 23.9 ka b2k, respectively). In agreement with Kocurek and Lancaster (1999), several factors may have influenced this time lag, such as (i) the amount of fine particles released by their respective sedimentary sources; (ii) the wind transport capacity; (iii) the local availability of sediments (role of vegetation and soil moisture). Among the various potential factors, fluctuations in the amount of particles available for deflation due to changes in ice sheet pattern appear to be a pivotal point that explains the chronological disparities between aeolian systems. For northern Europe, reconstructions show the following:

(1) During late MIS 3 (~ 35 ka b2k, GI-7), the area covered by the FIS was restricted to the Norwegian mountains (Hughes et al., 2016). During this period, sediment produced by glacial abrasion was transported by meltwater to a proglacial lake, the Baltic Lake (Lambeck et al., 2010) (**Fig. 6A**). A significant portion of the dust from the outwash was trapped by the lake. This pattern could explain the near absence of deposition in the E-NELB between ~60 ka b2k and 32 ka b2k (**Fig. 3B; Fig. 4**) and strengthens the ~30 ka hiatus hypothesis for LPS of Saxony suggested through high-resolution luminescence dating (Kreutzer et al., 2012; Meszner et al., 2013; Meszner and Faust, 2018). Simultaneously, the considerable growth of the BIIS (Clark et al., 2022) resulted in significant loess deposition in the W-NELB (**Fig. 4**).

(2) During MIS 2, the BIIS and FIS invaded the North Sea basin and merged into a single ice sheet, the European Ice Sheet (EIS) (Clark et al., 2012; Hughes et al., 2016; Batchelor et al., 2019) (**Fig. 6B**). Recent reconstructions of the ice extent in the North Sea suggest a coalescence of the BIIS and FIS at ca. 26 ka (e.g., Becker et al., 2018; Roberts et al., 2018; Clark et al., 2022). Coalescence resulted in the rerouting of meltwater produced by the FIS toward the North Atlantic via the Manche River, which then served as the primary drain for proglacial flows and for the Rhine, Seine, and Thames rivers (Toucanne et al., 2015; Patton et al., 2017). Analysis of the MD95-2002 marine core collected at the foot of the continental slope off Brittany indirectly allows dating the beginning of the development of the Manche mega-catchment (Toucanne et al., 2015). Fe/Ca and Ti/Ca ratios in sediments, which are proxies for terrigenous inputs, increased abruptly at ca. 31 ka b2k and kept high values until ca. 16.5 ka b2k despite some fluctuations (**Fig. 3D**). The onset of this phase is synchronous with the beginning of loess accumulation in the northern European plain (**Fig. 3B**) and the establishment of cold and relatively dry conditions on the European continent recorded by pollen assemblages (Fletcher et al., 2010; Duprat-Oualid et al., 2017) (**Fig. 3F**). The maximum of dust sedimentation is then concomitant with the maximal extension of the EIS around 23-21 ka b2k (Hughes et al., 2016; Patton et al., 2016) and reflects the peak of the inputs of glacial particles to proglacial rivers and the Manche River.

(3) Between ca. 19.9 ka and 17.5 ka, the rapid retreat of the ice sheet resulted in the splitting of BIIS and the FIS (**Fig. 6C**) (Becker et al., 2018; Evans et al., 2021). Catastrophic drainage of the North Sea ice-dammed lake south of the EIS has been dated to ca. 18.7 ka cal. BP (Hjelstuen et al., 2018). Much of the meltwater then flowed to the Norwegian Sea through the open gap between the two ice sheets, and the sedimentary load transported by the Manche River decreased drastically, limiting the amount of particles available for deflation in the W-NELB (Baykal et al., 2022). The rapid northward retreat of the FIS synchronously led to a sharp decrease in loess deposits in the E-NELB. For the NELB as a whole, this decrease was particularly significant after 18 ka b2k (**Fig. 3B**).

In comparison, palaeogeographic changes related to AIS fluctuations in response to climate change were less drastic than those of the EIS due to the smaller area and topographic constraints (Seguinot et al., 2018). Recent studies show the following:

(1) The AIS reached its maximal volume around 26-23 ka, i.e., during GS-3 (e.g., Preusser et al., 2011; Monegato et al., 2017; Ivy-Ochs et al., 2018; Gaar et al., 2019; Braakhekke et al., 2020; Kamleitner et al., 2022), or even earlier in the western Alps, i.e., between 40 ka and 30 ka (Gribenski et al., 2021). Isotope records from Alpine speleothems (Luetscher et al., 2015) (**Fig. 3E**) and climate simulations (Del Gobbo et al., 2022) provide evidence for moisture advection from the Mediterranean Sea to the Alps during GS-3, leading to rapid ice sheet growth. This stadial broadly corresponds to the coldest phase of the Last Glacial (e.g., Hughes and Gibbard, 2015) and coincides with the major peaks of dust accumulation in Greenland ice cores (Ruth et al., 2003; Rasmussen et al., 2014). It also coincides with the accumulation maximum recorded in PL (**Fig. 3C**).

(2) The AIS entered a recession phase after 22 ka and lost approximately 80% of its ice volume by 17.5 ka (e.g., Ivy-Ochs et al., 2008; Monegato et al., 2017). As a result, the age density of PL decreases sharply during GS-2 (**Fig. 3C**).

For each of the aeolian systems, the synchrony between loess deposition and the period of maximal glacier advance strongly suggests that the two processes are intimately related. The time lag between the maximal extension of the EIS and AIS, as well as the associated palaeogeographic changes, correctly accounts for the chronological differences between the emplacement of the NELB and PL.

For some authors (Stevens et al., 2020; Baykal et al., 2022), the increase in dust emissions would be largely correlated with the increase in meltwater fluxes during the recession phases of the EIS. Due to the signal smoothing created by the use of a wide bandwidth (imposed by the need to obtain a statistically reliable signal), our approach does not allow us to address this aspect very precisely. The results obtained here nevertheless suggest that, for each aeolian system, the main phase of loess sedimentation corresponded to the maximal advance of the glaciers, while rapid recession after 20 ka b2k led to a marked decrease in accumulation. Observations from contemporary temperate-based glaciers (Hallet et al., 1996; Jansson et al., 2005; Riihimaki et al., 2005) provide some basis for comparison. Overall, fine particle production, primarily by abrasion (e.g., Alley et al., 1997; Iverson et al., 1995; Riihimaki et al., 2005), increases in parallel with glacier size (see the conceptual model of Jansson et al., 2005), due to the larger areas of eroded bedrock and greater amounts of meltwater released in summer. Acceleration of basal slip, caused by increased water pressure in summer, promotes high particle production, which is then discharged into subglacial conduits (Riihimaki et al., 2005). By nature, the accelerated melting of a glacier causes only a transient increase in meltwater flows due to the correlative decrease in the amount of available ice. The geomorphic evolution of the glacier margin also largely influences the downstream transfer of particles (e.g., Knight et al., 2000). Proglacial lakes formed behind moraines and in over-deepened areas during the periods of glacier retreat tend to trap particles and reduce the load carried downstream. However, the periodic drainage of lakes and the redistribution of newly exposed sediments by slope processes introduce significant complexity to the system (e.g., Knight et al., 2000; Porter et al., 2010). In summary, the possibility of a correlation between ice sheet recession and increased loess sedimentation does not seem straightforward and remains to be studied in more detail.

4.2 MARs and loess thickness

The average MAR obtained in this study from 23 LPS reaches 792 g.m^{-2}.a^{-1} over the last 60 ka b2k (**Table 1**). Comparison
410   with literature data calculated with a similar method shows that these values are within the range of published MARs.
Schaffernicht et al. (2020) calculated a mean MAR of 811 g.m^{-2}.a^{-1} from 70 LPS distributed over Europe, which is close to our
estimate, while Újvári et al. (2010) and Albani et al. (2014) found slightly lower values, of 417 g.m^{-2}.a^{-1} ($n = 33$) and 569 g.m^{-2}.a^{-1} ($n = 15$), respectively. Much higher values were found, however, by Frechen et al. (2003), i.e., 1,675 g.m^{-2}.a^{-1} ($n = 23$),
but this may result from luminescence dating issues, as some of the methods used are now superseded.

415   Maximum MARs are more than three times higher than mean MARs (**Table 1**). These values exceed 2,000 g.m^{-2}.a^{-1} in eastern
Poland, the Carpathian basin, the Po valley and the Upper Rhine Graben, with a maximum of 4,993 g.m^{-2}.a^{-1} recorded at
Tyszowice (Poland) (**Fig. 7**). At Dunaszekcső (Hungary), our estimate of the highest MAR (3,058 g.m^{-2}.a^{-1}) agrees with that
obtained by Újvári et al. (2017) using a Bayesian age−depth model performed with the Bacon software (2,885 g.m^{-2}.a^{-1}).

As most of the Last Glacial loess accumulation occurred during the time interval used to calculate average MARs, a strong
420   correlation appears between MARs and loess thickness, as reported by, e.g., Bertran et al. (2021). The thickest deposits are
mainly located in the Upper Rhine Graben, the Lower Rhine Embayment, Saxony, Poland and the Carpathian Basin (Middle
Danube) and correspond well to areas where the highest MARs (>800 g.m^{-2}.a^{-1}) have been recorded (**Fig. 7**). The Bok section
located on Susak Island, bordering the Po Plain (Wacha et al., 2011) is also characterized by a substantial loess thickness and
a high mean MAR. Several hypotheses have been put forward to explain this spatial distribution:

425   (1) Except for Poland, the thickest loess accumulations are associated with rivers draining the AIS, suggesting that the
production of glacial particles was more efficient than for the FIS and BIIS (Bertran et al., 2021). Glacial abrasion occurs
under temperate and polythermal glaciers when ice slides over bedrock. The abrasion rate depends primarily on ice
velocity and thickness (modulating the pressure applied to the bed) and bedrock resistance (e.g., Hallet, 1979; Iverson,
1990; de Winter et al., 2012). These factors explain Alpine glaciers' high production of fine particles due to the steep
430   valley slopes and relatively soft bedrock, composed mainly of sedimentary rocks as opposed to the plutonic and
metamorphic basements of the Scandinavian shield. For Poland, simulations by Patton et al. (2016) reconstructed high ice
displacement velocities in the north of Poland (the Baltic Sea ice stream), which was favourable for glacial particle
production.

(2) Relief and vegetation cover played an important role in loess accumulation and probably contributed to the latitudinal
435   differences in loess thickness. In the low-relief plains of the NELB covered by herbaceous vegetation, loess deposits form
extensive blankets, whose thickness slowly decreases away from sources. In contrast, loess accumulated more locally in
southern Europe but often to a great thickness near the sources due to steeper relief and taller vegetation cover, efficiently
trapping the particles (Bosq et al., 2018; Bertran et al., 2021).

(3) A preservation bias possibly exists related to the depositional context of perialpine and NELB loess. Extensive erosional
440   unconformities and deeply incised valleys have been described in some loess sections from the NELB (e.g., Antoine et
al., 2001; Meijs, 2002; Lehmkuhl et al., 2016; Schirmer, 2016) and interpreted as of thermokarst origin (Antoine et al.,
2001; Kadereit et al., 2013), or more broadly, to reworking processes in a periglacial context (Lautridou et al., 1985;
Lehmkuhl et al., 2021). The formation of permafrost and repeated thermokarst processes generated large gaps in the
sedimentary record and may account in part for the lower mean MARs than in more southerly regions.

445   Examination of the period of maximum MAR value for each LPS shows significant disparities (**Fig. 8**). Two areas can be
distinguished, one corresponding to the NELB where ages are recent and relatively homogeneous, ranging from 29.9 ka b2k
to 18.4 ka b2k, and the other to the perialpine loess that shows greater heterogeneity, with ages spread over a longer period
(>60 ka b2k to 14.1 ka b2k). The combination of factors that could potentially explain this heterogeneity is the non-synchrony
of glacial advances in the Alpine massif depending on the valleys (e.g., Braakhekke et al., 2020; Gribenski et al., 2021;
450   Kamleitner et al., 2022) in agreement with simulations (Seguinot et al., 2018), and local sedimentation conditions. At the local

scale, loess accumulation and erosion would have been controlled by site specificity, particularly geomorphic location, topography, local winds, vegetation, and sediment availability in river floodplains (Bokhorst et al., 2011; Stevens et al., 2011; Fenn et al., 2021). Climatic changes could thus have had a significant impact in a context of more contrasted relief than for the Northern European plains.

455 **4.3 The future potential of the ChronoLoess database**

The idea of pooling luminescence data from literature and making them better accessible is not new, and efforts put in repositories such as the INQUA Dune Atlas (Lancaster et al., 2016) or *OCTOPUS* (Codilean et al., 2018, 2022) indicate a specific demand. Challenging remains that luminescence ages are not necessarily compatible across different studies. If used to derive broader implications, such as presented here, age values alone are insufficient, but all numerical values used for the
460 age calculations are required to avoid systematic deviations. Since we did not have access to the original data (measured physical quantities, such as luminescence), our approach is still non-perfect. However, for the first time, we attempted to extract all available data and combine them to render a bigger picture, here last Glacial loess history in Europe.
Beyond, our study, however, our data can be used for additional analyses such as for studies on the encountered environmental radioactivity.

465 **5 Conclusions**

The chronological study of European loess sections shows that the two major aeolian systems, the NELB on the one hand and the systems associated with the rivers draining the AIS on the other hand, did not develop synchronously. The significant deposition started at about 32 ka b2k for the NELB versus 42 ka b2k for the perialpine loess and peaked about two millennia later for the former (21.8 ka b2k vs 23.9 ka b2k, respectively). This shift resulted mainly from the time lag between the maxima
470 of the AIS and BIIS-FIS, which acted as the primary sources of fine-grained particles through glacial abrasion. The major geomorphic changes that resulted from the development and decay of the BIIS and FIS also played an important role. Particularly, ice sheet coalescence during the LGM diverted meltwater fluxes through the Manche River and provided huge amounts of glacial particles available for deflation in the W-NELB. The mean MAR obtained in this study from 23 LPS reaches 792 $g.m^{-2}.a^{-1}$ over the last 60 ka b2k and falls within the range of published values, while maximum MARs reach up to 4,993
475 $g.m^{-2}.a^{-1}$. The period during which the maximum MAR is recorded for each LPS is relatively homogeneous in the NELB and ranges from 30 ka b2k to 19 ka b2k, whereas it is more scattered in the perialpine systems (>60 ka b2k to 14 ka b2k). This probably resulted from a combination of factors, including the asynchrony of maximum valley glacier advances and local geomorphic factors. The ChronoLoess database will be extended over time as new data will become available.

Author contributions.

480 MB, PB and SK initiated the work and compiled data the dataset. MB extracted the luminescence ages from the original publication and prepared the first manuscript draft. PD and PL developed and validated the modelling tools. SK and CS validated the ChronoLoess datasets, added additional data and recalculated the ages. All authors contributed equally to the interpretation and discussion of the results and the revision of this manuscript.

Competing interests.

485 The authors declare that there is no conflict of interest.

Code and data availability.

All data described and presented in this contribution is available open-access at Zenodo, https://doi.org/10.5281/zenodo.7728616 (Bosq et al., 2023).

Acknowledgements.

490   We acknowledge Anaïs Vignoles for her help with the GIS data conversion, Julien Seguinot for AIS simulation data, and Samuel Toucanne for geochemical data from the MD95-2002 core.

Financial support.

This research benefitted from the support of multiple funding sources. This work was funded by the LaScArBx involving the universities of Bordeaux and Bordeaux-Montaigne (research program of Agence Nationale de la Recherche ANR-10-LABX-495   52) through the project ChronoLoess (PB dir.). Additional funding was also provided by the University of Lausanne (CS). PB was supported by the Institut National de Recherches Archéologiques Préventives (Inrap) and SK by the European Union's Horizon 2020 research and innovation programme (CREDit, grant no. 844457) while validating the luminescence database in 2020/2021. During the final revision and submission phase, SK was supported by the DFG Heisenberg programme (project id: 505822867).

500   **Review statement.**

This paper was reviewed by Zoran Perić and one anonymous referee.

References

Albani, S., Mahowald, N. M., Perry, A. T., Scanza, R. A., Zender, C. S., Heavens, N. G., Maggi, V., Kok, J. F., and Otto-Bliesner, B. L.: Improved dust representation in the Community Atmosphere Model, Journal of Advances in Modeling Earth 505   Systems, 6, 541–570, https://doi.org/10.1002/2013MS000279, 2014.

Albani, S., Mahowald, N. M., Winckler, G., Anderson, R. F., Bradtmiller, L. I., Delmonte, B., François, R., Goman, M., Heavens, N. G., Hesse, P. P., Hovan, S. A., Kang, S. G., Kohfeld, K. E., Lu, H., Maggi, V., Mason, J. A., Mayewski, P. A., McGee, D., Miao, X., Otto-Bliesner, B. L., Perry, A. T., Pourmand, A., Roberts, H. M., Rosenbloom, N., Stevens, T., and Sun, J.: Twelve thousand years of dust: the Holocene global dust cycle constrained by natural archives, Climate of the Past, 11, 510   869–903, https://doi.org/10.5194/cp-11-869-2015, 2015.

Alley, R. B., Cuffey, K. M., Evenson, E. B., Strasser, J. C., Lawson, D. E., and Larson, G. J.: How glaciers entrain and transport basal sediment: Physical constraints, Quaternary Science Reviews, 16, 1017–1038, https://doi.org/10.1016/S0277-3791(97)00034-6, 1997.

Amante, C. and Eakins, B. W.: ETOPO1 1 Arc-Minute Global Relief Model: Procedures, Data Sources and Analysis, 515   https://doi.org/10.7289/V5C8276M, 2009.

Antoine, P., Rousseau, D.-D., Zöller, L., Lang, A., Munaut, A.-V., Hatté, C., and Fontugne, M.: High-resolution record of the last Interglacial–glacial cycle in the Nussloch loess–palaeosol sequences, Upper Rhine Area, Germany, Quaternary International, 76–77, 211–229, https://doi.org/10.1016/S1040-6182(00)00104-X, 2001.

Antoine, P., Rousseau, D.-D., Moine, O., Kunesch, S., Hatté, C., Lang, A., Tissoux, H., and Zöller, L.: Rapid and cyclic aeolian 520   deposition during the Last Glacial in European loess: a high-resolution record from Nussloch, Germany, Quaternary Science Reviews, 28, 2955–2973, https://doi.org/10.1016/j.quascirev.2009.08.001, 2009.

Arnalds, O., Dagsson-Waldhauserova, P., and Olafsson, H.: The Icelandic volcanic aeolian environment: Processes and impacts — A review, Aeolian Research, 20, 176–195, https://doi.org/10.1016/j.aeolia.2016.01.004, 2016.

525 Avram, A., Constantin, D., Veres, D., Kelemen, S., Obreht, I., Hambach, U., Marković, S. B., and Timar-Gabor, A.: Testing polymineral post-IR IRSL and quartz SAR-OSL protocols on Middle to Late Pleistocene loess at Batajnica, Serbia, Boreas, 49, 615–633, https://doi.org/10.1111/bor.12442, 2020.

Batchelor, C. L., Margold, M., Krapp, M., Murton, D. K., Dalton, A. S., Gibbard, P. L., Stokes, C. R., Murton, J. B., and Manica, A.: The configuration of Northern Hemisphere ice sheets through the Quaternary, Nat Commun, 10, 3713, https://doi.org/10.1038/s41467-019-11601-2, 2019.

530 Bateman, M. D.: Handbook of luminescence dating, edited by: Bateman, M. D., Whittles Publishing, Dunbeath, 400 pp., 2019.

Baykal, Y., Stevens, T., Engström-Johansson, A., Skurzyński, J., Zhang, H., He, J., Lu, H., Adamiec, G., Költringer, C., and Jary, Z.: Detrital zircon U–Pb age analysis of last glacial loess sources and proglacial sediment dynamics in the Northern European Plain, Quaternary Science Reviews, 274, 107265, https://doi.org/10.1016/j.quascirev.2021.107265, 2021.

Baykal, Y., Stevens, T., Bateman, M. D., Pfaff, K., Sechi, D., Banak, A., Šuica, S., Zhang, H., and Nie, J.: Eurasian Ice Sheet
535 derived meltwater pulses and their role in driving atmospheric dust activity: Late Quaternary loess sources in SE England, Quaternary Science Reviews, 296, 107804, https://doi.org/10.1016/j.quascirev.2022.107804, 2022.

Becker, L. W. M., Sejrup, H. P., Hjelstuen, B. O., Haflidason, H., and Dokken, T. M.: Ocean-ice sheet interaction along the SE Nordic Seas margin from 35 to 15ka BP, Marine Geology, 402, 99–117, https://doi.org/10.1016/j.margeo.2017.09.003, 2018.

540 Beghin, P., Charbit, S., Dumas, C., Kageyama, M., and Ritz, C.: How might the North American ice sheet influence the northwestern Eurasian climate?, Climate of the Past, 11, 1467–1490, https://doi.org/10.5194/cp-11-1467-2015, 2015.

Bertran, P., Bosq, M., Borderie, Q., Coussot, C., Coutard, S., Deschodt, L., Franc, O., Gardère, P., Liard, M., and Wuscher, P.: Revised map of European aeolian deposits derived from soil texture data, Quaternary Science Reviews, 266, 107085, https://doi.org/10.1016/j.quascirev.2021.107085, 2021.

545 Bokhorst, M. P., Vandenberghe, J., Sümegi, P., Łanczont, M., Gerasimenko, N. P., Matviishina, Z. N., Marković, S. B., and Frechen, M.: Atmospheric circulation patterns in central and eastern Europe during the Weichselian Pleniglacial inferred from loess grain-size records, Quaternary International, 234, 62–74, https://doi.org/10.1016/j.quaint.2010.07.018, 2011.

Bosq, M., Bertran, P., Degeai, J.-P., Kreutzer, S., Queffelec, A., Moine, O., and Morin, E.: Last Glacial aeolian landforms and deposits in the Rhône Valley (SE France): Spatial distribution and grain-size characterization, Geomorphology, 318, 250–269,
550 https://doi.org/10.1016/j.geomorph.2018.06.010, 2018.

Bosq, M., Kreutzer, S., Bertran, P., Degeai, J.-P., Dugas, P., Kadereit, A., Lanos, P., Moine, O., Pfaffner, N., Queffelec, A., and Sauer, D.: Chronostratigraphy of two Late Pleistocene loess-palaeosol sequences in the Rhône Valley (southeast France), Quaternary Science Reviews, 245, 106473, https://doi.org/10.1016/j.quascirev.2020.106473, 2020a.

Bosq, M., Bertran, P., Degeai, J.-P., Queffelec, A., and Moine, O.: Geochemical signature of sources, recycling and weathering
555 in the Last Glacial loess from the Rhône Valley (southeast France) and comparison with other European regions, Aeolian Research, 42, 100561, https://doi.org/10.1016/j.aeolia.2019.100561, 2020b.

Bosq, M., Kreutzer, S., Bertran, P., Lanos, P., Dufresne, P., and Schmidt, C.: ChronLoess Database (v1.0.0), Zenodo, https://doi.org/10.5281/zenodo.7728616, 2023.

Bøtter-Jensen, L., Duller, G. A. T., Murray, A. S., and Banerjee, D.: Blue Light Emitting Diodes for Optical Stimulation of
560 Quartz in Retrospective Dosimetry and Dating, Radiation Protection Dosimetry, 84, 335–340, https://doi.org/10.1093/oxfordjournals.rpd.a032750, 1999.

Braakhekke, J., Ivy-Ochs, S., Monegato, G., Gianotti, F., Martin, S., Casale, S., and Christl, M.: Timing and flow pattern of the Orta Glacier (European Alps) during the Last Glacial Maximum, Boreas, 49, 315–332, https://doi.org/10.1111/bor.12427, 2020.

565 Bronk Ramsey, C. B.: Methods for Summarizing Radiocarbon Datasets, Radiocarbon, 59, 1809–1833, https://doi.org/10.1017/RDC.2017.108, 2017.

Buggle, B., Glaser, B., Zöller, L., Hambach, U., Marković, S., Glaser, I., and Gerasimenko, N.: Geochemical characterization and origin of Southeastern and Eastern European loesses (Serbia, Romania, Ukraine), Quaternary Science Reviews, 27, 1058–1075, https://doi.org/10.1016/j.quascirev.2008.01.018, 2008.

570 Bullard, J. E.: Contemporary glacigenic inputs to the dust cycle, Earth Surface Processes and Landforms, 38, 71–89, https://doi.org/10.1002/esp.3315, 2013.

Bullard, J. E. and Mockford, T.: Seasonal and decadal variability of dust observations in the Kangerlussuaq area, west Greenland, Arctic, Antarctic, and Alpine Research, 50, S100011, https://doi.org/10.1080/15230430.2017.1415854, 2018.

Buylaert, J. P., Jain, M., Murray, A. S., Thomsen, K. J., Thiel, C., and Sohbati, R.: A robust feldspar luminescence dating
575 method for Middle and Late Pleistocene sediments, Boreas, 41, 435–451, https://doi.org/10.1111/j.1502-3885.2012.00248.x, 2012.

Buylaert, J.-P., Újvári, G., Murray, A. S., Smedley, R. K., and Kook, M.: On the relationship between K concentration, grain size and dose in feldspar, Radiation Measurements, 120, 181–187, https://doi.org/10.1016/j.radmeas.2018.06.003, 2018.

Clark, C. D., Hughes, A. L. C., Greenwood, S. L., Jordan, C., and Sejrup, H. P.: Pattern and timing of retreat of the last British-
580 Irish Ice Sheet, Quaternary Science Reviews, 44, 112–146, https://doi.org/10.1016/j.quascirev.2010.07.019, 2012.

Clark, C. D., Ely, J. C., Hindmarsh, R. C. A., Bradley, S., Ignéczi, A., Fabel, D., Ó Cofaigh, C., Chiverrell, R. C., Scourse, J., Benetti, S., Bradwell, T., Evans, D. J. A., Roberts, D. H., Burke, M., Callard, S. L., Medialdea, A., Saher, M., Small, D., Smedley, R. K., Gasson, E., Gregoire, L., Gandy, N., Hughes, A. L. C., Ballantyne, C., Bateman, M. D., Bigg, G. R., Doole, J., Dove, D., Duller, G. A. T., Jenkins, G. T. H., Livingstone, S. L., McCarron, S., Moreton, S., Pollard, D., Praeg, D., Sejrup,
585 H. P., Van Landeghem, K. J. J., and Wilson, P.: Growth and retreat of the last British–Irish Ice Sheet, 31 000 to 15 000 years ago: the BRITICE-CHRONO reconstruction, Boreas, 51, 699–758, https://doi.org/10.1111/bor.12594, 2022.

Clopper, C. J. and Pearson, E. S.: The Use of Confidence or Fiducial Limits Illustrated in the Case of the Binomial, Biometrika, 26, 404–413, https://doi.org/10.2307/2331986, 1934.

Codilean, A. T., Munack, H., Cohen, T. J., Saktura, W. M., Gray, A., and Mudd, S. M.: OCTOPUS: an open cosmogenic
590 isotope and luminescence database, Earth System Science Data, 10, 2123–2139, https://doi.org/10.5194/essd-10-2123-2018, 2018.

Codilean, A. T., Munack, H., Saktura, W. M., Cohen, T. J., Jacobs, Z., Ulm, S., Hesse, P. P., Heyman, J., Peters, K. J., Williams, A. N., Saktura, R. B. K., Rui, X., Chishiro-Dennelly, K., and Panta, A.: OCTOPUS database (v.2), Earth System Science Data, 14, 3695–3713, https://doi.org/10.5194/essd-14-3695-2022, 2022.

595 Constantin, D., Cameniță, A., Panaiotu, C., Necula, C., Codrea, V., and Timar-Gabor, A.: Fine and coarse-quartz SAR-OSL dating of Last Glacial loess in Southern Romania, Quaternary International, 357, 33–43, https://doi.org/10.1016/j.quaint.2014.07.052, 2015.

Contreras, D. A. and Meadows, J.: Summed radiocarbon calibrations as a population proxy: a critical evaluation using a realistic simulation approach, Journal of Archaeological Science, 52, 591–608, https://doi.org/10.1016/j.jas.2014.05.030,
600 2014.

Del Gobbo, C., Colucci, R. R., Monegato, G., Žebre, M., and Giorgi, F.: Atmosphere-cryosphere interactions at 21 ka BP in the European Alps, Climate of the Past Discussions, 1–24, https://doi.org/10.5194/cp-2022-43, 2022.

Dietrich, S. and Seelos, K.: The reconstruction of easterly wind directions for the Eifel region (Central Europe) during the period 40.3-12.9 ka BP, Climate of the Past, 6, 145–154, https://doi.org/10.5194/cp-6-145-2010, 2010.

605 Dijkmans, J. W. A. and Törnqvist, T. E.: Modern Periglacial Eolian Deposits and Landforms in the Sondre Stromfjord Area, West Greenland and Their Palaeoenvironmental Implications, Museum Tusculanum Press, 44 pp., 1991.

DKE/K 967: DIN/TS 44808-1:2022-03, Chronometrische Datierung mittels Lumineszenz in Geowissenschaften und Archäologie - Teil 1: Berichterstattung von Äquivalentdosen und Altersbestimmung, Beuth Verlag GmbH, https://doi.org/10.31030/3319499, 2022.

610 Duller, G. A. T.: Luminescence Dating: guidelines on using luminescence dating in archaeology, 2008.

Duller, G. A. T., Bøtter-Jensen, L., Kohsiek, P., and Murray, A. S.: A High-Sensitivity Optically Stimulated Luminescence Scanning System for Measurement of Single Sand-Sized Grains, Radiation Protection Dosimetry, 84, 325–330, https://doi.org/10.1093/oxfordjournals.rpd.a032748, 1999a.

Duller, G. A. T., Bøtter-Jensen, L., Murray, A. S., and Truscott, A. J.: Single grain laser luminescence (SGLL) measurements
615 using a novel automated reader, Nuclear Instruments and Methods in Physics Research Section B: Beam Interactions with Materials and Atoms, 155, 506–514, https://doi.org/10.1016/S0168-583X(99)00488-7, 1999b.

Duprat-Oualid, F., Rius, D., Bégeot, C., Magny, M., Millet, L., Wulf, S., and Appelt, O.: Vegetation response to abrupt climate changes in Western Europe from 45 to 14.7k cal a BP: the Bergsee lacustrine record (Black Forest, Germany), Journal of Quaternary Science, 32, 1008–1021, https://doi.org/10.1002/jqs.2972, 2017.

620   Durcan, J. A., King, G. E., and Duller, G. A. T.: DRAC: Dose Rate and Age Calculator for trapped charge dating, Quaternary Geochronology, 28, 54–61, https://doi.org/10.1016/j.quageo.2015.03.012, 2015.

Ehlers, J. and Gibbard, P. L.: Quaternary Glaciations - Extent and Chronology: Part I: Europe, Elsevier, Amsterdam, 489 pp., 2004.

Evans, D. J. A., Roberts, D. H., Bateman, M. D., Clark, C. D., Medialdea, A., Callard, L., Grimoldi, E., Chiverrell, R. C., Ely, 625   J., Dove, D., Ó Cofaigh, C., Saher, M., Bradwell, T., Moreton, S. G., Fabel, D., and Bradley, S. L.: Retreat dynamics of the eastern sector of the British–Irish Ice Sheet during the last glaciation, Journal of Quaternary Science, 36, 723–751, https://doi.org/10.1002/jqs.3275, 2021.

Fenn, K., Durcan, J. A., Thomas, D. S. G., Millar, I. L., and Marković, S. B.: Re-analysis of late Quaternary dust mass accumulation rates in Serbia using new luminescence chronology for loess–palaeosol sequence at Surduk, Boreas, 49, 634–630   652, https://doi.org/10.1111/bor.12445, 2020.

Fenn, K., Thomas, D. S. G., Durcan, J. A., Millar, I. L., Veres, D., Piermattei, A., and Lane, C. S.: A tale of two signals: Global and local influences on the Late Pleistocene loess sequences in Bulgarian Lower Danube, Quaternary Science Reviews, 274, 107264, https://doi.org/10.1016/j.quascirev.2021.107264, 2021.

Fletcher, W. J., Sánchez Goñi, M. F., Allen, J. R. M., Cheddadi, R., Combourieu-Nebout, N., Huntley, B., Lawson, I., Londeix, 635   L., Magri, D., Margari, V., Müller, U. C., Naughton, F., Novenko, E., Roucoux, K., and Tzedakis, P. C.: Millennial-scale variability during the last glacial in vegetation records from Europe, Quaternary Science Reviews, 29, 2839–2864, https://doi.org/10.1016/j.quascirev.2009.11.015, 2010.

Frechen, M., Oches, E. A., and Kohfeld, K. E.: Loess in Europe—mass accumulation rates during the Last Glacial Period, Quaternary Science Reviews, 22, 1835–1857, https://doi.org/10.1016/S0277-3791(03)00183-5, 2003.

640   Fuchs, M., Kreutzer, S., Rousseau, D.-D., Antoine, P., Hatté, C., Lagroix, F., Moine, O., Gauthier, C., Svoboda, J., and Lisá, L.: The loess sequence of Dolní Věstonice, Czech Republic: A new OSL-based chronology of the Last Climatic Cycle, Boreas, 42, 664–677, https://doi.org/10.1111/j.1502-3885.2012.00299.x, 2013.

Gaar, D., Graf, H. R., and Preusser, F.: New chronological constraints on the timing of Late Pleistocene glacier advances in northern Switzerland, E&G Quaternary Science Journal, 68, 53–73, https://doi.org/10.5194/egqsj-68-53-2019, 2019.

645   Gilks, W. R., Richardson, S., and Spiegelhalter, D.: Markov Chain Monte Carlo in Practice, Chapman&Hall., Chapman & Hall/CRC, London, 505 pp., 1995.

Green, P. J. and Silverman, B. W.: Nonparametric Regression and Generalized Linear Models: A roughness penalty approach, Chapman & Hall/CRC, London, 198 pp., 1993.

Gribenski, N., Valla, P. G., Preusser, F., Roattino, T., Crouzet, C., and Buoncristiani, J.-F.: Out-of-phase Late Pleistocene 650   glacial maxima in the Western Alps reflect past changes in North Atlantic atmospheric circulation, Geology, 49, 1096–1101, https://doi.org/10.1130/G48688.1, 2021.

Guérin, G., Antoine, P., Schmidt, E., Goval, E., Hérisson, D., Jamet, G., Reyss, J.-L., Shao, Q., Philippe, A., Vibet, M.-A., and Bahain, J.-J.: Chronology of the Upper Pleistocene loess sequence of Havrincourt (France) and associated Palaeolithic occupations: A Bayesian approach from pedostratigraphy, OSL, radiocarbon, TL and ESR/U-series data, Quaternary 655   Geochronology, 42, 15–30, https://doi.org/10.1016/j.quageo.2017.07.001, 2017.

Hallet, B., Hunter, L., and Bogen, J.: Rates of erosion and sediment evacuation by glaciers: A review of field data and their implications, Global and Planetary Change, 12, 213–235, https://doi.org/10.1016/0921-8181(95)00021-6, 1996.

Hallet, H.: A Theoretical Model of Glacial Abrasion, Journal of Glaciology, 23, 39–50, https://doi.org/10.3189/S0022143000029725, 1979.

660   Hjelstuen, B. O., Sejrup, H. P., Valvik, E., and Becker, L. W. M.: Evidence of an ice-dammed lake outburst in the North Sea during the last deglaciation, Marine Geology, 402, 118–130, https://doi.org/10.1016/j.margeo.2017.11.021, 2018.

Hugenholtz, C. H. and Wolfe, S. A.: Rates and environmental controls of aeolian dust accumulation, Athabasca River Valley, Canadian Rocky Mountains, Geomorphology, 121, 274–282, https://doi.org/10.1016/j.geomorph.2010.04.024, 2010.

Hughes, A. L. C., Gyllencreutz, R., Lohne, Ø. S., Mangerud, J., and Svendsen, J. I.: The last Eurasian ice sheets – a chronological database and time-slice reconstruction, DATED-1, Boreas, 45, 1–45, https://doi.org/10.1111/bor.12142, 2016.

Hughes, P. D. and Gibbard, P. L.: A stratigraphical basis for the Last Glacial Maximum (LGM), Quaternary International, 383, 174–185, https://doi.org/10.1016/j.quaint.2014.06.006, 2015.

Huntley, D. J. and Hancock, R. G. V.: The Rb contents of the K-feldspar grains being measured in optical dating, Ancient TL, 19, 43–46, 2001.

Huntley, D. J., Godfrey-Smith, D. I., and Thewalt, M. L. W.: Optical dating of sediments, Nature, 313, 105–107, https://doi.org/10.1038/313105a0, 1985.

Hütt, G., Jaek, I., and Tchonka, J.: Optical dating: K-Feldspars optical response stimulation spectra, Quaternary Science Reviews, 7, 381–385, https://doi.org/10.1016/0277-3791(88)90033-9, 1988.

Iverson, N. R.: Laboratory Simulations Of Glacial Abrasion: Comparison With Theory, Journal of Glaciology, 36, 304–314, https://doi.org/10.3189/002214390793701264, 1990.

Iverson, N. R., Hanson, B., Hooke, R. LeB., and Jansson, P.: Flow Mechanism of Glaciers on Soft Beds, Science, 267, 80–81, https://doi.org/10.1126/science.267.5194.80, 1995.

Ivy-Ochs, S., Kerschner, H., Reuther, A., Preusser, F., Heine, K., Maisch, M., Kubik, P. W., and Schlüchter, C.: Chronology of the last glacial cycle in the European Alps, Journal of Quaternary Science, 23, 559–573, https://doi.org/10.1002/jqs.1202, 2008.

Ivy-Ochs, S., Lucchesi, S., Baggio, P., Fioraso, G., Gianotti, F., Monegato, G., Graf, A. A., Akçar, N., Christl, M., Carraro, F., Forno, M. G., and Schlüchter, C.: New geomorphological and chronological constraints for glacial deposits in the Rivoli-Avigliana end-moraine system and the lower Susa Valley (Western Alps, NW Italy), Journal of Quaternary Science, 33, 550–562, https://doi.org/10.1002/jqs.3034, 2018.

Jansson, P., Rosqvist, G., and Schneider, T.: Glacier Fluctuations, Suspended Sediment Flux and Glacio-Lacustrine Sediments, Geografiska Annaler: Series A, Physical Geography, 87, 37–50, https://doi.org/10.1111/j.0435-3676.2005.00243.x, 2005.

Kadereit, A., Kind, C.-J., and Wagner, G. A.: The chronological position of the Lohne Soil in the Nussloch loess section – re-evaluation for a European loess-marker horizon, Quaternary Science Reviews, 59, 67–86, https://doi.org/10.1016/j.quascirev.2012.10.026, 2013.

Kageyama, M., Harrison, S. P., Kapsch, M.-L., Lofverstrom, M., Lora, J. M., Mikolajewicz, U., Sherriff-Tadano, S., Vadsaria, T., Abe-Ouchi, A., Bouttes, N., Chandan, D., Gregoire, L. J., Ivanovic, R. F., Izumi, K., LeGrande, A. N., Lhardy, F., Lohmann, G., Morozova, P. A., Ohgaito, R., Paul, A., Peltier, W. R., Poulsen, C. J., Quiquet, A., Roche, D. M., Shi, X., Tierney, J. E., Valdes, P. J., Volodin, E., and Zhu, J.: The PMIP4 Last Glacial Maximum experiments: preliminary results and comparison with the PMIP3 simulations, Climate of the Past, 17, 1065–1089, https://doi.org/10.5194/cp-17-1065-2021, 2021.

Kamleitner, S., Ivy-Ochs, S., Monegato, G., Gianotti, F., Akçar, N., Vockenhuber, C., Christl, M., and Synal, H.-A.: The Ticino-Toce glacier system (Swiss-Italian Alps) in the framework of the Alpine Last Glacial Maximum, Quaternary Science Reviews, 279, 107400, https://doi.org/10.1016/j.quascirev.2022.107400, 2022.

Kasse, C.: Cold-Climate Aeolian Sand-Sheet Formation in North-Western Europe (c. 14–12.4 ka); a Response to Permafrost Degradation and Increased Aridity, Permafrost and Periglacial Processes, 8, 295–311, https://doi.org/10.1002/(SICI)1099-1530(199709)8:3<295::AID-PPP256>3.0.CO;2-0, 1997.

King, G. E., Burow, C., Roberts, H. M., and Pearce, N. J. G.: Age determination using feldspar: Evaluating fading-correction model performance, Radiation Measurements, 119, 58–73, https://doi.org/10.1016/j.radmeas.2018.07.013, 2018.

Klasen, N., Fischer, P., Lehmkuhl, F., and Hilgers, A.: Luminescence dating of loess deposits from the Remagen-Schwalbenberg site, Western Germany, Geochronometria, 42, https://doi.org/10.1515/geochr-2015-0008, 2015.

Knight, P. G., Waller, R. I., Patterson, C. J., Jones, A. P., and Robinson, Z. P.: Glacier advance, ice-marginal lakes and routing of meltwater and sediment: Russell Glacier, Greenland, Journal of Glaciology, 46, 423–426, https://doi.org/10.3189/172756500781833160, 2000.

Kocurek, G. and Lancaster, N.: Aeolian system sediment state: theory and Mojave Desert Kelso dune field example, Sedimentology, 46, 505–515, https://doi.org/10.1046/j.1365-3091.1999.00227.x, 1999.

Kohfeld, K. E. and Harrison, S. P.: Glacial-interglacial changes in dust deposition on the Chinese Loess Plateau, Quaternary Science Reviews, 22, 1859–1878, https://doi.org/10.1016/S0277-3791(03)00166-5, 2003.

Kreutzer, S., Fuchs, M., Meszner, S., and Faust, D.: OSL chronostratigraphy of a loess-palaeosol sequence in Saxony/Germany using quartz of different grain sizes, Quaternary Geochronology, 10, 102–109, https://doi.org/10.1016/j.quageo.2012.01.004, 2012.

Kreutzer, S., Burow, C., Dietze, M., Fuchs, M. C., Fischer, M., and Schmidt, C.: Software in the context of luminescence dating: status, concepts and suggestions exemplified by the R package `Luminescence', Ancient TL, 35, 1–11, 2017.

Lambeck, K., Purcell, A., Zhao, J., and SVENSSON, N.-O.: The Scandinavian ice sheet: from MIS 4 to the end of the last glacial maximum, Boreas, 39, 410–435, https://doi.org/10.1111/j.1502-3885.2010.00140.x, 2010.

Lambeck, K., Rouby, H., Purcell, A., Sun, Y., and Sambridge, M.: Sea level and global ice volumes from the Last Glacial Maximum to the Holocene, Proceedings of the National Academy of Sciences, 111, 15296–15303, https://doi.org/10.1073/pnas.1411762111, 2014.

Lancaster, N., Wolfe, S., Thomas, D., Bristow, C., Bubenzer, O., Burrough, S., Duller, G., Halfen, A., Hesse, P., Roskin, J., Singhvi, A., Tsoar, H., Tripaldi, A., Yang, X., and Zárate, M.: The INQUA Dunes Atlas chronologic database, Quaternary International, 410, 3–10, https://doi.org/10.1016/j.quaint.2015.10.044, 2016.

Lanos, P.: Bayesian Inference of Calibration Curves: Application to Archaeomagnetism, in: Tools for Constructing Chronologies: Crossing Disciplinary Boundaries, vol. 177, edited by: Buck, C. E. and Millard, A. R., Springer, London, 43–82, https://doi.org/10.1007/978-1-4471-0231-1_3, 2004.

Lanos, P. and Dufresne, P.: ChronoModel version 2.0 User manual, 2019.

Lanos, P. and Dufresne, P.: Composer le temps en archéologie avec ChronoModel, in: Mesurer le temps de l'Age du Bronze, edited by: Marcigny, C., Lachenal, T., and Milcent, P.-Y., Saint-Germain-en-Laye, 49–72, 2022.

Lanos, P. and Philippe, A.: Event Date Model: A Robust Bayesian Tool for Chronology Building, Communications for Statistical Applications and Methods (CSAM), 158, 131–157, https://doi.org/10.29220/csam.2018.25.2.131, 2017a.

Lanos, P. and Philippe, A.: Hierarchical Bayesian modeling for combining dates in archeological context, Journal de la société française de statistique, 158, 72–88, 2017b.

Lautridou, J.-P., Sommé, J., Heim, J., Puisségur, J.-J., and Rousseau, D.-D.: La stratigraphie des loess et formations fluviatiles d'Achenheim (Alsace): nouvelles données bioclimatiques et corrélations avec les séquences pléistocènes de la France du Nord-Ouest, Quaternaire, 22, 125–132, 1985.

Lehmkuhl, F., Zens, J., Krauß, L., Schulte, P., and Kels, H.: Loess-paleosol sequences at the northern European loess belt in Germany: Distribution, geomorphology and stratigraphy, Quaternary Science Reviews, 153, 11–30, https://doi.org/10.1016/j.quascirev.2016.10.008, 2016.

Lehmkuhl, F., Nett, J. J., Pötter, S., Schulte, P., Sprafke, T., Jary, Z., Antoine, P., Wacha, L., Wolf, D., Zerboni, A., Hošek, J., Marković, S. B., Obreht, I., Sümegi, P., Veres, D., Zeeden, C., Boemke, B., Schaubert, V., Viehweger, J., and Hambach, U.: Loess landscapes of Europe – Mapping, geomorphology, and zonal differentiation, Earth-Science Reviews, 215, 103496, https://doi.org/10.1016/j.earscirev.2020.103496, 2021.

Löfverström, M., Caballero, R., Nilsson, J., and Kleman, J.: Evolution of the large-scale atmospheric circulation in response to changing ice sheets over the last glacial cycle, Climate of the Past, 10, 1453–1471, https://doi.org/10.5194/cp-10-1453-2014, 2014.

Lomax, J., Fuchs, M., Preusser, F., and Fiebig, M.: Luminescence based loess chronostratigraphy of the Upper Palaeolithic site Krems-Wachtberg, Austria, Quaternary International, 351, 88–97, https://doi.org/10.1016/j.quaint.2012.10.037, 2014.

Ludwig, P., Schaffernicht, E. J., Shao, Y., and Pinto, J. G.: Regional atmospheric circulation over Europe during the Last Glacial Maximum and its links to precipitation, Journal of Geophysical Research: Atmospheres, 121, 2130–2145, https://doi.org/10.1002/2015JD024444, 2016.

Luetscher, M., Boch, R., Sodemann, H., Spötl, C., Cheng, H., Edwards, R. L., Frisia, S., Hof, F., and Müller, W.: North Atlantic storm track changes during the Last Glacial Maximum recorded by Alpine speleothems, Nat Commun, 6, 6344, https://doi.org/10.1038/ncomms7344, 2015.

Mahan, S. A., Rittenour, T. M., Nelson, M. S., Ataee, N., Brown, N., DeWitt, R., Durcan, J., Evans, M., Feathers, J., Frouin, M., Guérin, G., Heydari, M., Huot, S., Jain, M., Keen-Zebert, A., Li, B., López, G. I., Neudorf, C., Porat, N., Rodrigues, K., Sawakuchi, A. O., Spencer, J. Q. G., and Thomsen, K.: Guide for interpreting and reporting luminescence dating results, GSA Bulletin, https://doi.org/10.1130/B36404.1, 2022.

760 Meijs, E. P. M.: Loess stratigraphy in Dutch and Belgian Limburg, E&G Quaternary Science Journal, 51, 115–131, https://doi.org/10.3285/eg.51.1.08, 2002.

Mejdahl, V.: Internal radioactivity in quartz and feldspar grains, Ancient TL, 5, 10–17, 1987.

Meszner, S. and Faust, D.: Paläoböden in den Lössgebieten Ostdeutschlands, in: Handbuch der Bodenkunde, edited by: Blume, H.-P., Stahr, K., Fisher, W., Guggenberger, G., Horn, R., Frede, H.-G., and Felix-Henningsen, P., John Wiley & Sons, Ltd, 1–765 20, 2018.

Meszner, S., Kreutzer, S., Fuchs, M., and Faust, D.: Late Pleistocene landscape dynamics in Saxony, Germany: Paleoenvironmental reconstruction using loess-paleosol sequences, Quaternary International, 296, 94–107, https://doi.org/10.1016/j.quaint.2012.12.040, 2013.

Moine, O., Antoine, P., Hatté, C., Landais, A., Mathieu, J., Prud'homme, C., and Rousseau, D.-D.: The impact of Last Glacial 770 climate variability in west-European loess revealed by radiocarbon dating of fossil earthworm granules, Proceedings of the National Academy of Sciences, 114, 6209–6214, https://doi.org/10.1073/pnas.1614751114, 2017.

Moine, O., Antoine, P., Coutard, S., Guérin, G., Hatté, C., Paris, C., and Saulnier-Copard, S.: Intra-interstadial environmental changes in Last Glacial loess revealed by molluscan assemblages from the Upper Palaeolithic site of Amiens-Renancourt 1 (Somme, France), Journal of Quaternary Science, 36, 1322–1340, https://doi.org/10.1002/jqs.3312, 2021.

775 Monegato, G., Scardia, G., Hajdas, I., Rizzini, F., and Piccin, A.: The Alpine LGM in the boreal ice-sheets game, Sci Rep, 7, 2078, https://doi.org/10.1038/s41598-017-02148-7, 2017.

Moska, P., Jary, Z., Adamiec, G., and Bluszcz, A.: OSL chronostratigraphy of a loess-palaeosol sequence in Złota using quartz and polymineral fine grains, Radiation Measurements, 81, 23–31, https://doi.org/10.1016/j.radmeas.2015.04.012, 2015.

Moska, P., Adamiec, G., Jary, Z., and Bluszcz, A.: OSL chronostratigraphy for loess deposits from Tyszowce – Poland, 780 Geochronometria, Vol. 44, https://doi.org/10.1515/geochr-2015-0074, 2017.

Moska, P., Jary, Z., Adamiec, G., and Bluszcz, A.: Chronostratigraphy of a loess-palaeosol sequence in Biały Kościół, Poland using OSL and radiocarbon dating, Quaternary International, 502, 4–17, https://doi.org/10.1016/j.quaint.2018.05.024, 2019a.

Moska, P., Jary, Z., Adamiec, G., and Bluszcz, A.: High resolution dating of loess profile from Strzyżów (Horodło Plateau-Ridge, Volhynia Upland), Quaternary International, 502, 18–29, https://doi.org/10.1016/j.quaint.2018.02.016, 2019b.

785 Murray, A. S. and Wintle, A. G.: Luminescence dating of quartz using an improved single-aliquot regenerative-dose protocol, Radiation Measurements, 32, 57–73, https://doi.org/10.1016/s1350-4487(99)00253-x, 2000.

Patton, H., Hubbard, A., Andreassen, K., Winsborrow, M., and Stroeven, A. P.: The build-up, configuration, and dynamical sensitivity of the Eurasian ice-sheet complex to Late Weichselian climatic and oceanic forcing, Quaternary Science Reviews, 153, 97–121, https://doi.org/10.1016/j.quascirev.2016.10.009, 2016.

790 Patton, H., Hubbard, A., Andreassen, K., Auriac, A., Whitehouse, P. L., Stroeven, A. P., Shackleton, C., Winsborrow, M., Heyman, J., and Hall, A. M.: Deglaciation of the Eurasian ice sheet complex, Quaternary Science Reviews, 169, 148–172, https://doi.org/10.1016/j.quascirev.2017.05.019, 2017.

Perić, Z., Lagerbäck Adolphi, E., Stevens, T., Újvári, G., Zeeden, C., Buylaert, J.-P., Marković, S. B., Hambach, U., Fischer, P., Schmidt, C., Schulte, P., Huayu, L., Shuangwen, Y., Lehmkuhl, F., Obreht, I., Veres, D., Thiel, C., Frechen, M., Jain, M., 795 Vött, A., Zöller, L., and Gavrilov, M. B.: Quartz OSL dating of late quaternary Chinese and Serbian loess: A cross Eurasian comparison of dust mass accumulation rates, Quaternary International, 502, 30–44, https://doi.org/10.1016/j.quaint.2018.01.010, 2019.

Perić, Z. M., Marković, S. B., Avram, A., Timar-Gabor, A., Zeeden, C., Nett, J. J., Fischer, P., Fitzsimmons, K. E., and Gavrilov, M. B.: Initial quartz OSL and dust mass accumulation rate investigation of the Kisiljevo loess sequence in north-800 eastern Serbia, Quaternary International, 620, 13–23, https://doi.org/10.1016/j.quaint.2020.10.040, 2022.

Pinto, J. G. and Ludwig, P.: Extratropical cyclones over the North Atlantic and western Europe during the Last Glacial Maximum and implications for proxy interpretation, Climate of the Past, 16, 611–626, https://doi.org/10.5194/cp-16-611-2020, 2020.

805 Porter, P. R., Vatne, G., Ng, F., and Irvine-Fynn, T. D. l.: Ice-Marginal Sediment Delivery to the Surface of a High-Arctic Glacier: Austre Brøggerbreen, Svalbard, Geografiska Annaler: Series A, Physical Geography, 92, 437–449, https://doi.org/10.1111/j.1468-0459.2010.00406.x, 2010.

Preusser, F., Graf, H. R., Keller, O., Krayss, E., and Schlüchter, C.: Quaternary glaciation history of northern Switzerland, E&G Quaternary Science Journal, 60, 282–305, https://doi.org/10.3285/eg.60.2-3.06, 2011.

Rasmussen, S. O., Bigler, M., Blockley, S. P., Blunier, T., Buchardt, S. L., Clausen, H. B., Cvijanovic, I., Dahl-Jensen, D.,
810 Johnsen, S. J., Fischer, H., Gkinis, V., Guillevic, M., Hoek, W. Z., Lowe, J. J., Pedro, J. B., Popp, T., Seierstad, I. K., Steffensen, J. P., Svensson, A. M., Vallelonga, P., Vinther, B. M., Walker, M. J. C., Wheatley, J. J., and Winstrup, M.: A stratigraphic framework for abrupt climatic changes during the Last Glacial period based on three synchronized Greenland ice-core records: refining and extending the INTIMATE event stratigraphy, Quaternary Science Reviews, 106, 14–28, https://doi.org/10.1016/j.quascirev.2014.09.007, 2014.

815 Reimer, P. J., Austin, W. E. N., Bard, E., Bayliss, A., Blackwell, P. G., Ramsey, C. B., Butzin, M., Cheng, H., Edwards, R. L., Friedrich, M., Grootes, P. M., Guilderson, T. P., Hajdas, I., Heaton, T. J., Hogg, A. G., Hughen, K. A., Kromer, B., Manning, S. W., Muscheler, R., Palmer, J. G., Pearson, C., Plicht, J. van der, Reimer, R. W., Richards, D. A., Scott, E. M., Southon, J. R., Turney, C. S. M., Wacker, L., Adolphi, F., Büntgen, U., Capano, M., Fahrni, S. M., Fogtmann-Schulz, A., Friedrich, R., Köhler, P., Kudsk, S., Miyake, F., Olsen, J., Reinig, F., Sakamoto, M., Sookdeo, A., and Talamo, S.: The IntCal20 Northern
820 Hemisphere Radiocarbon Age Calibration Curve (0–55 cal kBP), Radiocarbon, 62, 725–757, https://doi.org/10.1017/RDC.2020.41, 2020.

Riihimaki, C. A., MacGregor, K. R., Anderson, R. S., Anderson, S. P., and Loso, M. G.: Sediment evacuation and glacial erosion rates at a small alpine glacier, Journal of Geophysical Research: Earth Surface, 110, https://doi.org/10.1029/2004JF000189, 2005.

825 Rivoirard, V. and Stoltz, G.: Statistique mathématique en action, Vuibert, 2012.

Roberts, D. H., Evans, D. J. A., Callard, S. L., Clark, C. D., Bateman, M. D., Medialdea, A., Dove, D., Cotterill, C. J., Saher, M., Cofaigh, C. Ó., Chiverrell, R. C., Moreton, S. G., Fabel, D., and Bradwell, T.: Ice marginal dynamics of the last British-Irish Ice Sheet in the southern North Sea: Ice limits, timing and the influence of the Dogger Bank, Quaternary Science Reviews, 198, 181–207, https://doi.org/10.1016/j.quascirev.2018.08.010, 2018.

830 Rousseau, D.-D., Sima, A., Antoine, P., Hatté, C., Lang, A., and Zöller, L.: Link between European and North Atlantic abrupt climate changes over the last glaciation, Geophysical Research Letters, 34, https://doi.org/10.1029/2007GL031716, 2007.

Rousseau, D.-D., Svensson, A., Bigler, M., Sima, A., Steffensen, J. P., and Boers, N.: Eurasian contribution to the last glacial dust cycle: how are loess sequences built?, Climate of the Past, 13, 1181–1197, https://doi.org/10.5194/cp-13-1181-2017, 2017.

835 Rousseau, D.-D., Antoine, P., and Sun, Y.: How dusty was the last glacial maximum over Europe?, Quaternary Science Reviews, 254, 106775, https://doi.org/10.1016/j.quascirev.2020.106775, 2021.

Ruth, U., Wagenbach, D., Steffensen, J. P., and Bigler, M.: Continuous record of microparticle concentration and size distribution in the central Greenland NGRIP ice core during the last glacial period, Journal of Geophysical Research: Atmospheres, 108, https://doi.org/10.1029/2002JD002376, 2003.

840 Sanchez Goñi, M. F. and Harrison, S. P.: Millennial-scale climate variability and vegetation changes during the Last Glacial: Concepts and terminology, Quaternary Science Reviews, 29, 2823–2827, https://doi.org/10.1016/j.quascirev.2009.11.014, 2010.

Schaffernicht, E. J., Ludwig, P., and Shao, Y.: Linkage between dust cycle and loess of the Last Glacial Maximum in Europe, Atmospheric Chemistry and Physics, 20, 4969–4986, https://doi.org/10.5194/acp-20-4969-2020, 2020.

845 Scheidt, S., Berg, S., Hambach, U., Klasen, N., Pötter, S., Stolz, A., Veres, D., Zeeden, C., Brill, D., Brückner, H., Kusch, S., Laag, C., Lehmkuhl, F., Melles, M., Monnens, F., Oppermann, L., Rethemeyer, J., and Nett, J. J.: Chronological Assessment of the Balta Alba Kurgan Loess-Paleosol Section (Romania) – A Comparative Study on Different Dating Methods for a Robust and Precise Age Model, Frontiers in Earth Science, 8, 2021.

Schirmer, W.: Late Pleistocene loess of the Lower Rhine, Quaternary International, 411, 44–61, https://doi.org/10.1016/j.quaint.2016.01.034, 2016.

Seguinot, J., Ivy-Ochs, S., Jouvet, G., Huss, M., Funk, M., and Preusser, F.: Modelling last glacial cycle ice dynamics in the Alps, The Cryosphere, 12, 3265–3285, https://doi.org/10.5194/tc-12-3265-2018, 2018.

Sitzia, L., Bertran, P., Sima, A., Chery, P., Queffelec, A., and Rousseau, D.-D.: Dynamics and sources of last glacial aeolian deposition in southwest France derived from dune patterns, grain-size gradients and geochemistry, and reconstruction of efficient wind directions, Quaternary Science Reviews, 170, 250–268, https://doi.org/10.1016/j.quascirev.2017.06.029, 2017.

Skurzyński, J., Jary, Z., Kenis, P., Kubik, R., Moska, P., Raczyk, J., and Seul, C.: Geochemistry and mineralogy of the Late Pleistocene loess-palaeosol sequence in Złota (near Sandomierz, Poland): Implications for weathering, sedimentary recycling and provenance, Geoderma, 375, 114459, https://doi.org/10.1016/j.geoderma.2020.114459, 2020.

Smalley, I. J. and Leach, J. A.: The origin and distribution of the loess in the Danube basin and associated regions of East-Central Europe — A review, Sedimentary Geology, 21, 1–26, https://doi.org/10.1016/0037-0738(78)90031-3, 1978.

Stadelmaier, K. H., Ludwig, P., Bertran, P., Antoine, P., Shi, X., Lohmann, G., and Pinto, J. G.: A new perspective on permafrost boundaries in France during the Last Glacial Maximum, Climate of the Past, 17, 2559–2576, https://doi.org/10.5194/cp-17-2559-2021, 2021.

Stevens, T., Marković, S. B., Zech, M., Hambach, U., and Sümegi, P.: Dust deposition and climate in the Carpathian Basin over an independently dated last glacial–interglacial cycle, Quaternary Science Reviews, 30, 662–681, https://doi.org/10.1016/j.quascirev.2010.12.011, 2011.

Stevens, T., Sechi, D., Bradák, B., Orbe, R., Baykal, Y., Cossu, G., Tziavaras, C., Andreucci, S., and Pascucci, V.: Abrupt last glacial dust fall over southeast England associated with dynamics of the British-Irish ice sheet, Quaternary Science Reviews, 250, 106641, https://doi.org/10.1016/j.quascirev.2020.106641, 2020.

Sümegi, P., Gulyás, S., Molnár, D., Szilágyi, G., Sümegi, B. P., Törőcsik, T., and Molnár, M.: 14C Dated Chronology of the Thickest and Best Resolved Loess/Paleosol Record of the LGM from SE Hungary Based on Comparing Precision and Accuracy of Age-Depth Models, Radiocarbon, 62, 403–417, https://doi.org/10.1017/RDC.2019.154, 2020.

Summerfield, M. A.: Global Geomorphology, Routledge, London, 560 pp., https://doi.org/10.4324/9781315841182, 2014.

Thomsen, K. J., Murray, A. S., Jain, M., and Bøtter-Jensen, L.: Laboratory fading rates of various luminescence signals from feldspar-rich sediment extracts, Radiation Measurements, 43, 1474–1486, https://doi.org/10.1016/j.radmeas.2008.06.002, 2008.

Timar, A., Vandenberghe, D., Panaiotu, E. C., Panaiotu, C. G., Necula, C., Cosma, C., and van den haute, P.: Optical dating of Romanian loess using fine-grained quartz, Quaternary Geochronology, 5, 143–148, https://doi.org/10.1016/j.quageo.2009.03.003, 2010.

Toucanne, S., Soulet, G., Freslon, N., Jacinto, R. S., Dennielou, B., Zaragosi, S., Eynaud, F., Bourillet, J.-F., and Bayon, G.: Millennial-scale fluctuations of the European Ice Sheet at the end of the last glacial, and their potential impact on global climate, Quaternary Science Reviews, 123, 113–133, https://doi.org/10.1016/j.quascirev.2015.06.010, 2015.

Toucanne, S., Soulet, G., Vázquez Riveiros, N., Boswell, S. M., Dennielou, B., Waelbroeck, C., Bayon, G., Mojtahid, M., Bosq, M., Sabine, M., Zaragosi, S., Bourillet, J.-F., and Mercier, H.: The North Atlantic Glacial Eastern Boundary Current as a Key Driver for Ice-Sheet—AMOC Interactions and Climate Instability, Paleoceanography and Paleoclimatology, 36, e2020PA004068, https://doi.org/10.1029/2020PA004068, 2021.

Újvári, G., Varga, A., and Balogh-Brunstad, Z.: Origin, weathering, and geochemical composition of loess in southwestern Hungary, Quaternary Research, 69, 421–437, https://doi.org/10.1016/j.yqres.2008.02.001, 2008.

Újvári, G., Kovács, J., Varga, G., Raucsik, B., and Marković, S. B.: Dust flux estimates for the Last Glacial Period in East Central Europe based on terrestrial records of loess deposits: a review, Quaternary Science Reviews, 29, 3157–3166, https://doi.org/10.1016/j.quascirev.2010.07.005, 2010.

Újvári, G., Molnár, M., and Páll-Gergely, B.: Charcoal and mollusc shell 14C-dating of the Dunaszekcső loess record, Hungary, Quaternary Geochronology, 35, 43–53, https://doi.org/10.1016/j.quageo.2016.05.005, 2016.

Újvári, G., Stevens, T., Molnár, M., Demény, A., Lambert, F., Varga, G., Jull, A. T., Páll-Gergely, B., Buylaert, J.-P., and Kovács, J.: Coupled European and Greenland last glacial dust activity driven by North Atlantic climate, Proceedings of the National Academy of Sciences, 114, E10632–E10638, https://doi.org/10.1073/pnas.171265111, 2017.

Vermeesch, P.: On the visualisation of detrital age distributions, Chemical Geology, 312–313, 190–194, https://doi.org/10.1016/j.chemgeo.2012.04.021, 2012.

Wacha, L., Mikulčić Pavlaković, S., Frechen, M., and Crnjaković, M.: The Loess Chronology of the Island of Susak, Croatia, E&G Quaternary Science Journal, 60, 153–169, https://doi.org/10.3285/eg.60.1.11, 2011.

Wallinga, J., Murray, A., and Wintle, A.: The single-aliquot regenerative-dose (SAR) protocol applied to coarse-grain feldspar, Radiation Measurements, 32, 529–533, https://doi.org/10.1016/s1350-4487(00)00091-3, 2000.

de Winter, I. L., Storms, J. E. A., and Overeem, I.: Numerical modeling of glacial sediment production and transport during deglaciation, Geomorphology, 167–168, 102–114, https://doi.org/10.1016/j.geomorph.2012.05.023, 2012.

Wolf, D., Kolb, T., Alcaraz-Castaño, M., Heinrich, S., Baumgart, P., Calvo, R., Sánchez, J., Ryborz, K., Schäfer, I., Bliedtner, M., Zech, R., Zöller, L., and Faust, D.: Climate deteriorations and Neanderthal demise in interior Iberia, Sci Rep, 8, 7048, https://doi.org/10.1038/s41598-018-25343-6, 2018.

Zeeberg, J.: The European sand belt in eastern Europe - and comparison of Late Glacial dune orientation with GCM simulation results, Boreas, 27, 127–139, https://doi.org/10.1111/j.1502-3885.1998.tb00873.x, 1998.

Zens, J., Schulte, P., Klasen, N., Krauß, L., Pirson, S., Burow, C., Brill, D., Eckmeier, E., Kels, H., Zeeden, C., Spagna, P., and Lehmkuhl, F.: OSL chronologies of paleoenvironmental dynamics recorded by loess-paleosol sequences from Europe: Case studies from the Rhine-Meuse area and the Neckar Basin, Palaeogeography, Palaeoclimatology, Palaeoecology, 509, 105–125, https://doi.org/10.1016/j.palaeo.2017.07.019, 2018.

Zickel, M., Becker, D., Verheul, J., Yener, Y., and Willmes, C.: Paleocoastlines GIS dataset. CRC806-Database, https://doi.org/10.5880/SFB806.20, 2016.

Table 1: Average sedimentation and mass accumulation rates from Bayesian age-depth modelling of 23 LPS during the last 60 ka **b2k**. Data sources: Balta Alba Kurgan (Scheidt et al., 2021); Batajnica (Avram et al., 2020); Biały Kościół (Moska et al., 2019a); Bok (Wacha et al., 2011); Collias (Bosq et al., 2020a); Dolní Věstonice (Fuchs et al., 2013); Dunaszekcső (Újvári et al., 2017); Krems Wachtberg (Lomax et al., 2014); Lautagne (Bosq et al., 2020a); Lunca (Constantin et al., 2015); Madaras (Sümegi et al., 2020); Mircea Vodă (Timar et al., 2010); Nussloch (Moine et al., 2017); Ostrau (Kreutzer et al., 2012); Pegwell Bay (Stevens et al., 2020); Schwalbenberg II (Klasen et al., 2015); Seilitz (Meszner et al., 2013); Slivata 1 (Fenn et al., 2021); Slivata 2 (Fenn et al., 2021); Strzyżów (Moska et al., 2019b); Tyszowce (Moska et al., 2017); Veliki Surduk (Perić et al., 2019); Złota (Moska et al., 2015).

N°	Site	Latitude (°N)	Longitude (°E)	Area	Dating method	SR mean (mm a^{-1})	Mass Accumulation Rate (MAR)			References
							mean (g m^{-2} a^{-1})	maximum (g m^{-2} a^{-1})	age of max. (ka b2k)	
1	Balta Alba Kurgan	45.278	27.291	Lower Danube	Luminescence and ^{14}C	0.24	356	658	32.4	Scheidt et al. (2021)
2	Batajnica	44.925	20.320	Carpathian basin	Luminescence	0.14	208	239	32.3	Avram et al. (2020)
3	Biały Kościół	50.730	17.020	Poland	Luminescence and ^{14}C	0.19	285	1222	23.1	Moska et al. (2019)
4	Bok	44.508	14.316	Po	Luminescence and ^{14}C	1.15	1724	3197	14.1	Wacha et al. (2011)
5	Collias	43.954	4.479	Rhone	Luminescence and ^{14}C	0.08	125	183	61.2	Bosq et al. (2020)
6	Dolní Věstonice	49.076	16.911	Moravia	Luminescence and ^{14}C	0.24	353	1488	20.9	Fuchs et al. (2013)
7	Dunaszekcső	46.090	18.760	Carpathian basin	Radiocarbon	0.96	1434	3058	24.6	Újvári et al. (2017)
8	Krems Wachtberg	48.400	15.583	Upper Danube	Luminescence and ^{14}C	0.35	524	823	20.1	Lomax et al. (2014)
9	Lautagne	44.904	4.897	Rhone	Luminescence and ^{14}C	0.21	309	786	27.8	Bosq et al. (2020)
10	Lunca	43.849	24.766	Lower Danube	Luminescence	0.07	105	153	34.9	Constantin et al. (2015)
11	Madaras	46.037	19.288	Carpathian basin	Radiocarbon	0.70	1054	1987	20.6	Sümegi et al. (2020)
12	Mircea Vodă	44.321	28.189	Lower Danube	Luminescence	0.05	77	150	71.8	Timar et al. (2010)
13	Nussloch	49.316	8.732	Upper Rhine	Radiocarbon	0.56	845	2319	24.3	Moine et al. (2017)
14	Ostrau	51.360	13.180	Saxony	Luminescence	0.58	875	1005	29.9	Kreutzer et al. (2012)
15	Pegwell Bay	51.328	1.370	England	Luminescence	0.12	179	337	23.6	Stevens et al. (2020)
16	Schwalbenberg II	50.561	7.245	Middle Rhine	Luminescence	1.20	1804	1849	18.4	Klasen et al. (2015)
17	Seilitz	51.360	13.433	Saxony	Luminescence	0.76	1138	1250	19.3	Meszner et al. (2013)
18	Slivata1	43.767	23.080	Lower Danube	Luminescence	0.96	1447	1506	23.5	Fenn et al. (2021)
19	Slivata2	43.763	23.058	Lower Danube	Luminescence	0.24	358	404	28.1	Fenn et al. (2021)
20	Strzyżów	50.851	24.008	Poland	Luminescence and ^{14}C	1.45	2181	2384	19.1	Moska et al. (2019)
21	Tyszowce	50.608	23.712	Poland	Luminescence and ^{14}C	1.14	1710	4993	19.1	Moska et al. (2017)
22	Veliki Surduk	45.300	20.190	Carpathian basin	Luminescence	0.21	322	502	46.7	Perić et al. (2019)
23	Złota	50.650	21.660	Poland	Luminescence and ^{14}C	0.54	809	1598	24.1	Moska et al. (2015)
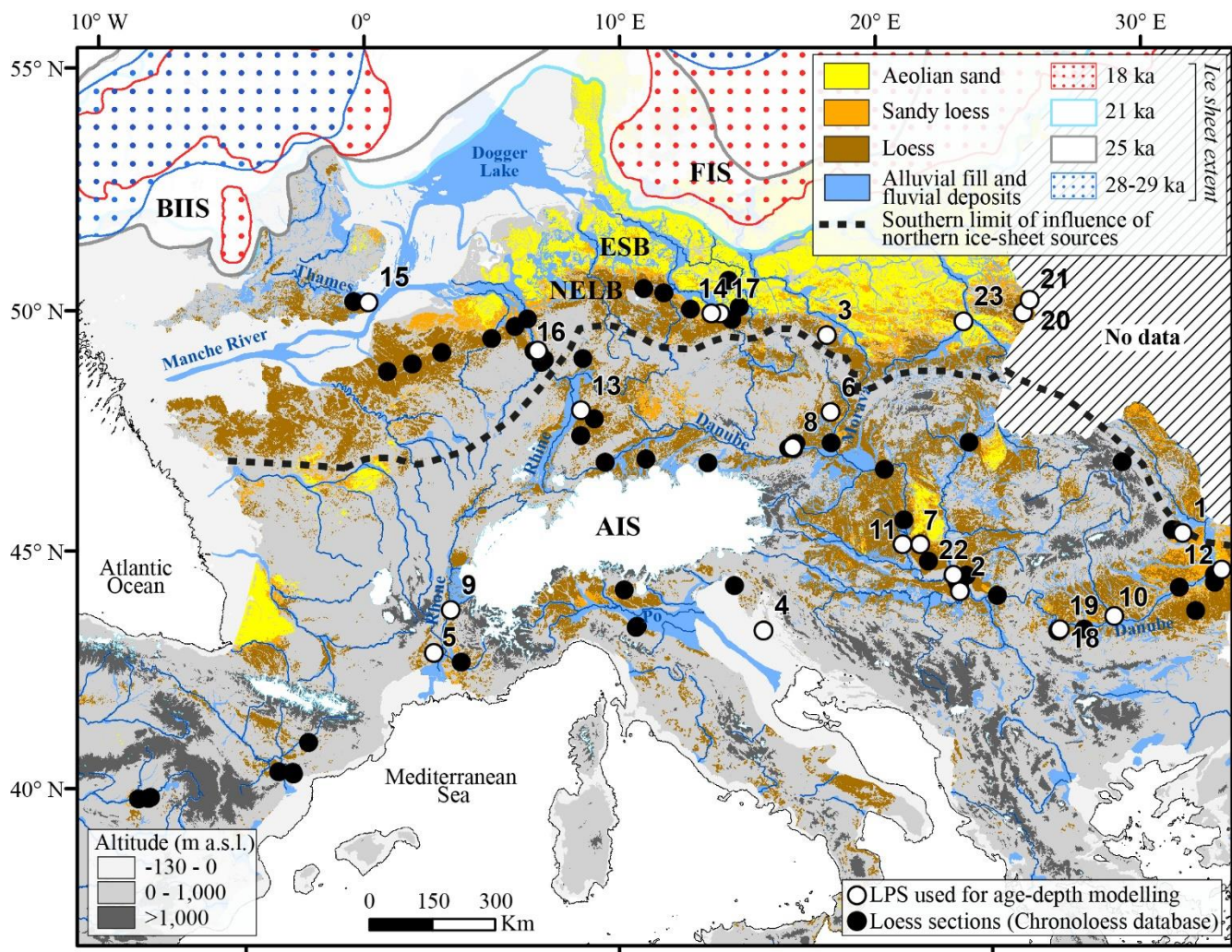
Figure 1: Palaeogeographic map of European aeolian deposits from Bertran et al. (2021) showing the location of the LPS used in the ChronoLoess database and those used for age-depth calculation. The British-Irish Ice Sheet (BIIS) and Fennoscandinavian Ice Sheet (FIS) are from Hughes et al. (2016). The Alpine Ice Sheet (AIS) and other LGM glaciers are from Ehlers and Gibbard (2004). The -130 m coastline is from Zickel et al. (2016). The map is based on the ETOPO1 Digital Elevation Model (Amante and Eakins, 2009). List of sites used for age-depth modelling: 1- Balta Alba Kurgan; 2- Batajnica; 3- Biały Kościół; 4- Bok; 5- Collias; 6- Dolní Věstonice; 7- Dunaszekcső; 8- Krems Wachtberg; 9- Lautagne; 10- Lunca; 11- Madaras; 12- Mircea Vodǎ; 13- Nussloch; 14- Ostrau; 15- Pegwell Bay; 16- Schwalbenberg II; 17- Seilitz; 18- Slivata 1; 19- Slivata 2; 20- Strzyżów; 21- Tyszowce; 22- Veliki Surduk; 23- Złota.
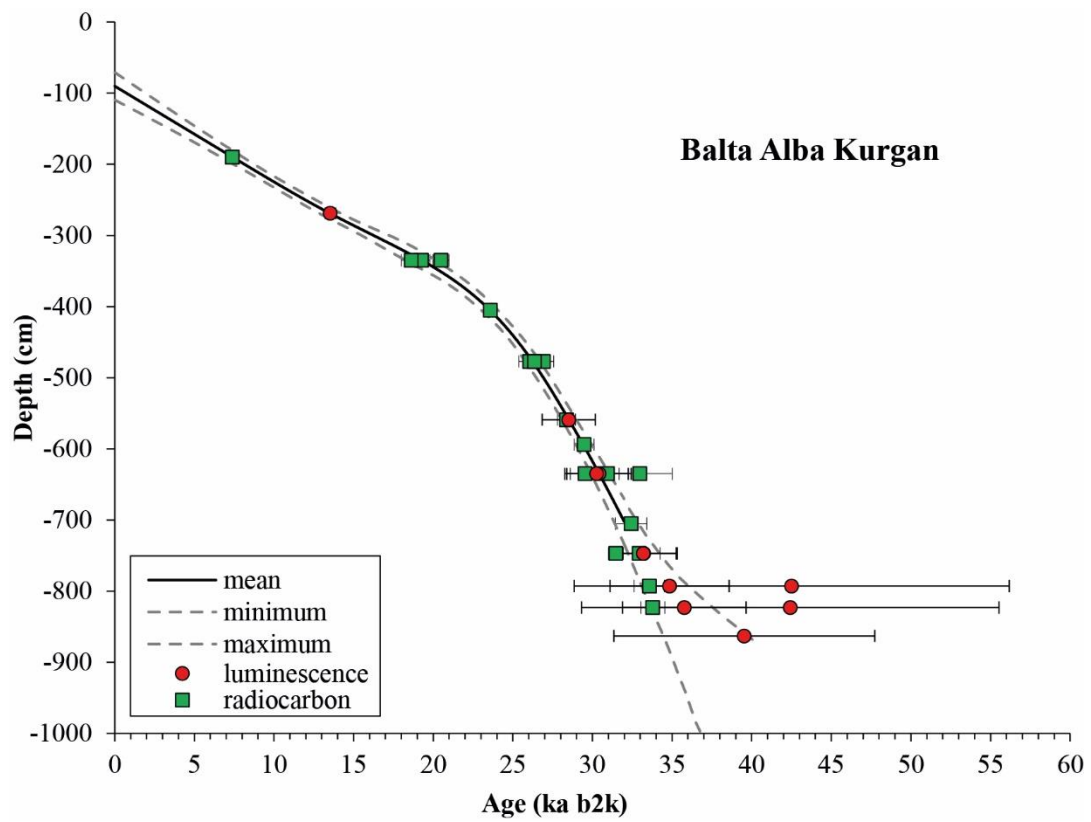
Figure 2: Example Bayesian age-depth model of Balta Alba Kurgan LPS from *ChronoModel*.
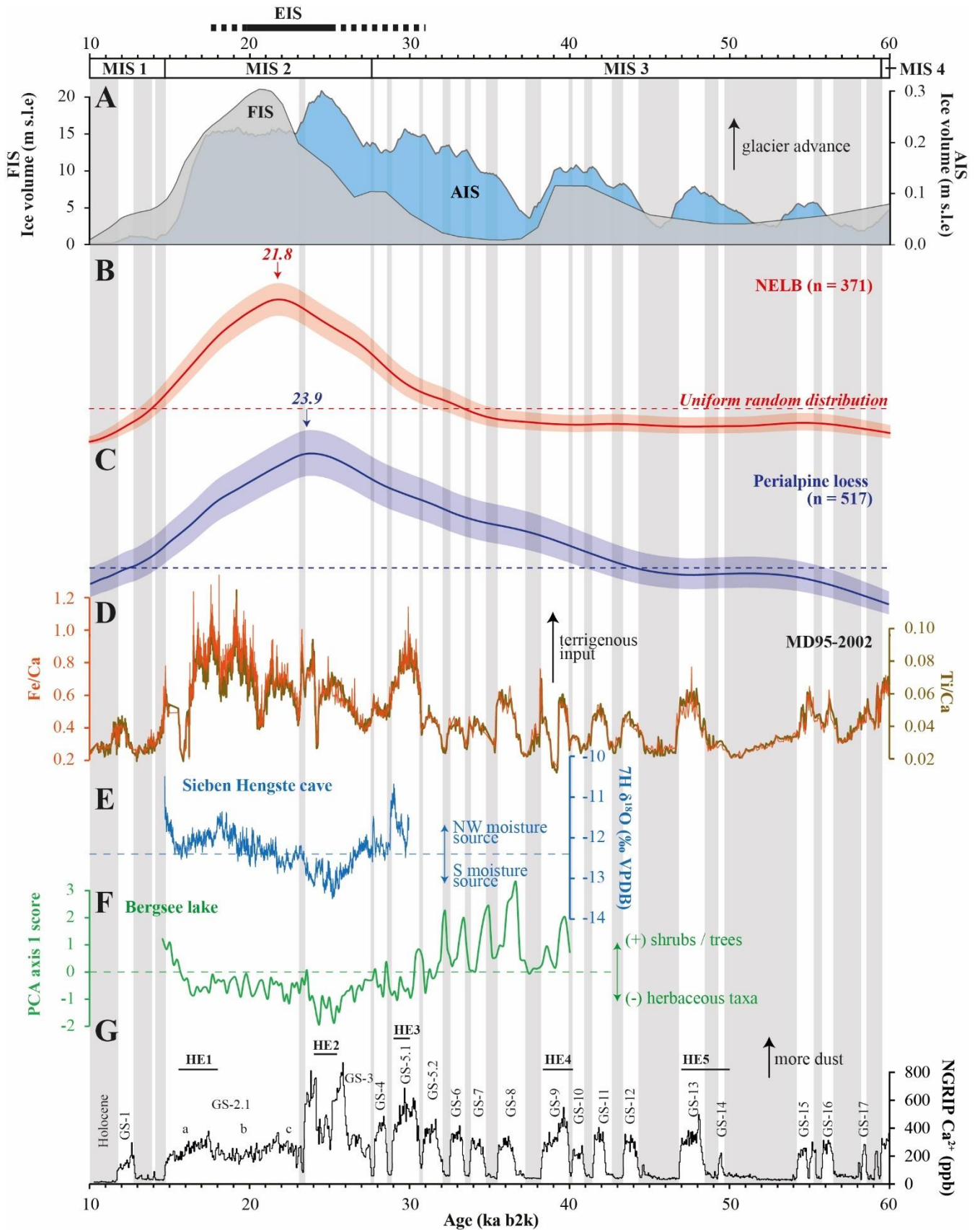
940

Figure 3: Comparison between ice and sediments records. A) AIS and FIS ice volume between 60 ka b2k and 10 ka b2k from simulations (Seguinot et al., 2018 and Lambeck et al., 2010). Modelled ice volumes are expressed in meters sea-level equivalent (m s.l.e.). B, C) Time-activity curves for the NELB (red) and perialpine loess (blue); the coloured bands indicate the 95% confidence interval and the dotted lines indicate the uniform random distribution. D) Fe/Ca and Ti/Ca ratios from MD95-2002 core off Brittany (Toucanne et al., 2015, 2021). E)
945 Score of principal component analysis (PCA) axis-1 for pollen data from Bergsee Lake (south Germany) (Duprat-Oualid et al., 2017). F) Sieben Hängste (7H) composite stalagmite δ^{18}O record (Western Alps) (Luetscher et al., 2015) .G) NGRIP Ca^{2+} data over the last 60 ka b2k (Rasmussen et al., 2014). The MIS and Heinrich Events (HEs) are from Sanchez Goñi and Harrison (2010).
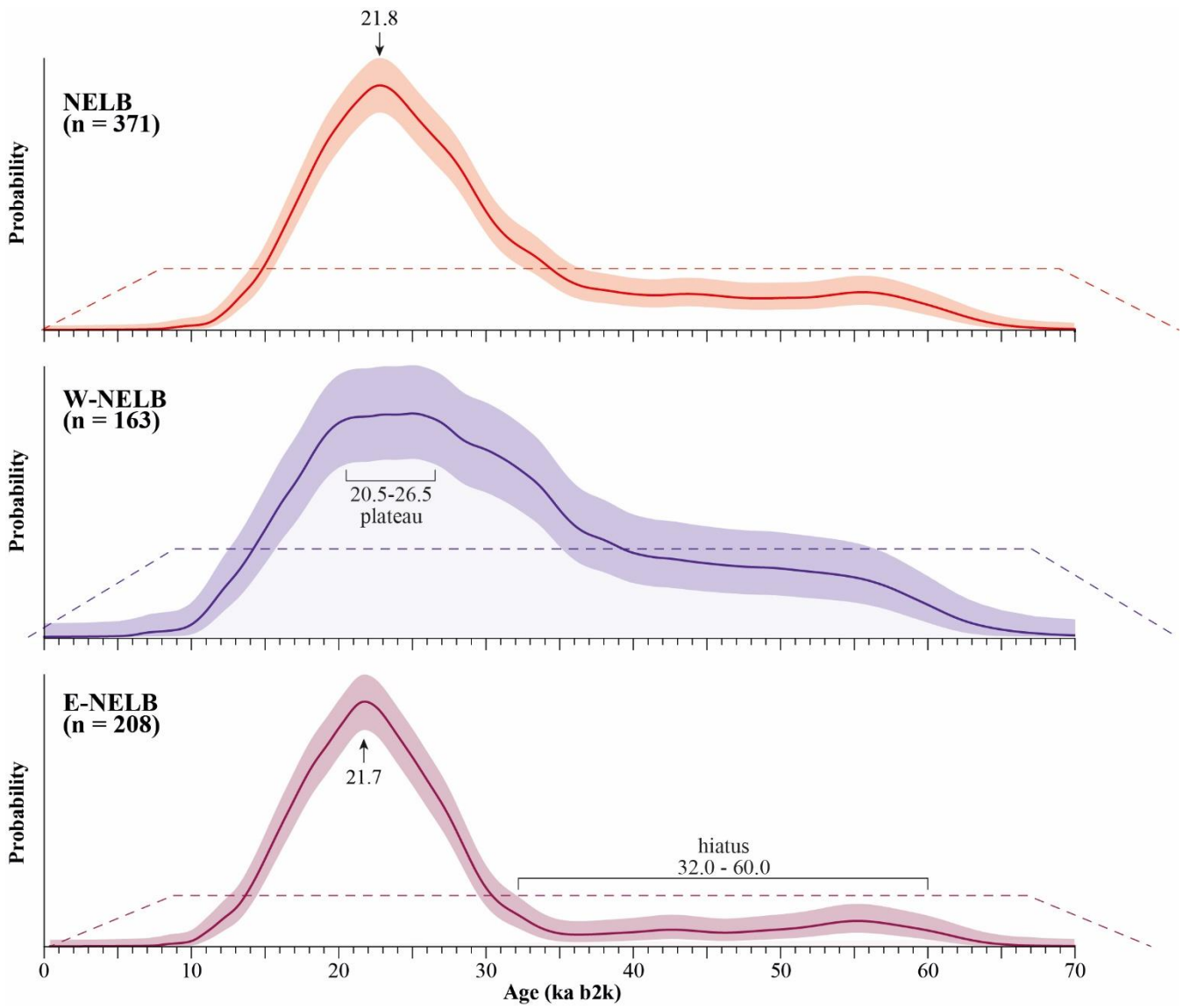
Figure 4: Time-activity curves for the NELB, W-NELB (Belgium, Southern England, North France, West-Germany) and E-NELB (Southern Poland, East Germany). The coloured bands indicate the 95% confidence interval and the dotted lines indicate the uniform random distribution.
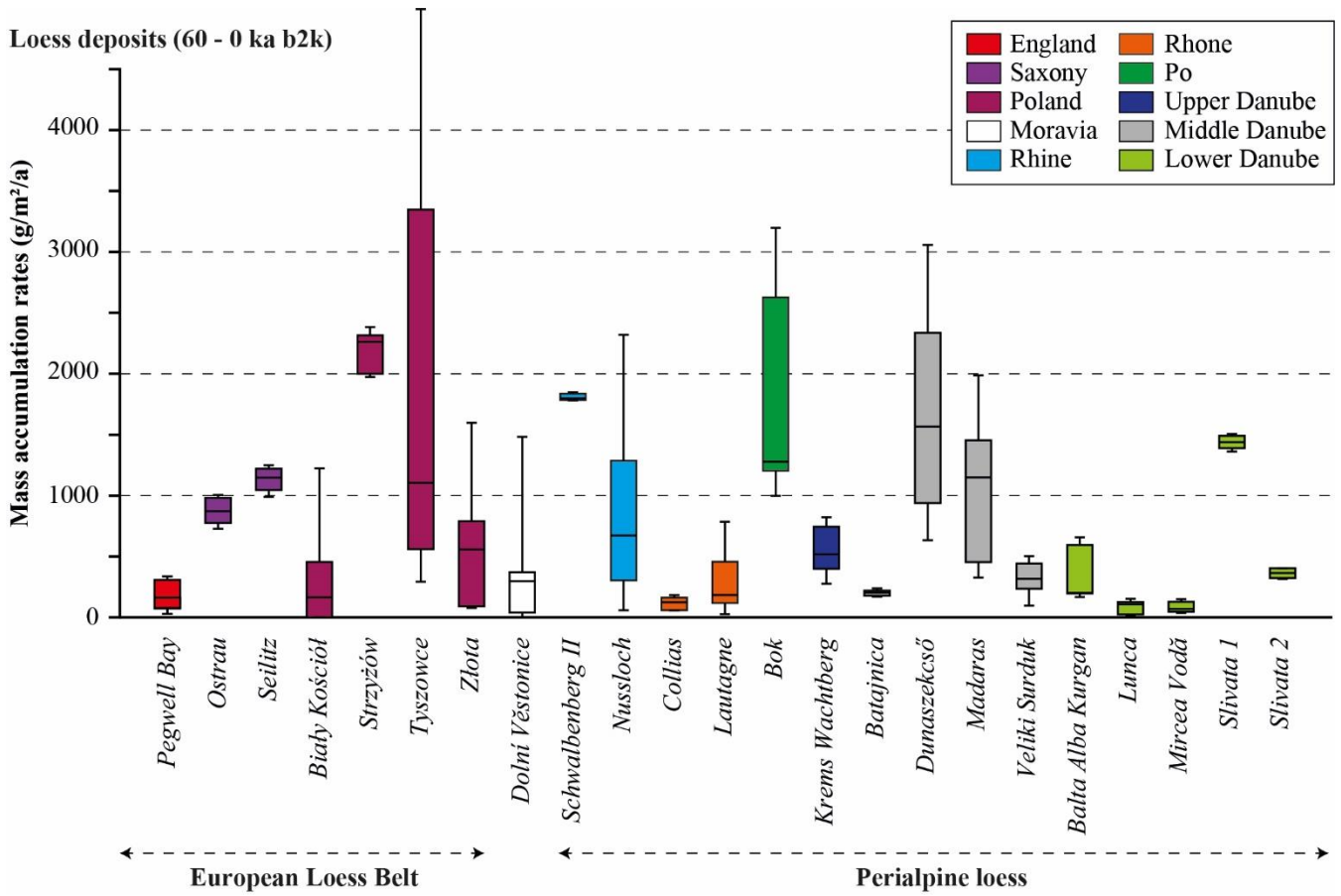
Figure 5: Box plot of MARs derived from age-depth modelling of some European LPS between 60 - 0 ka b2k (references in **Table 1**).
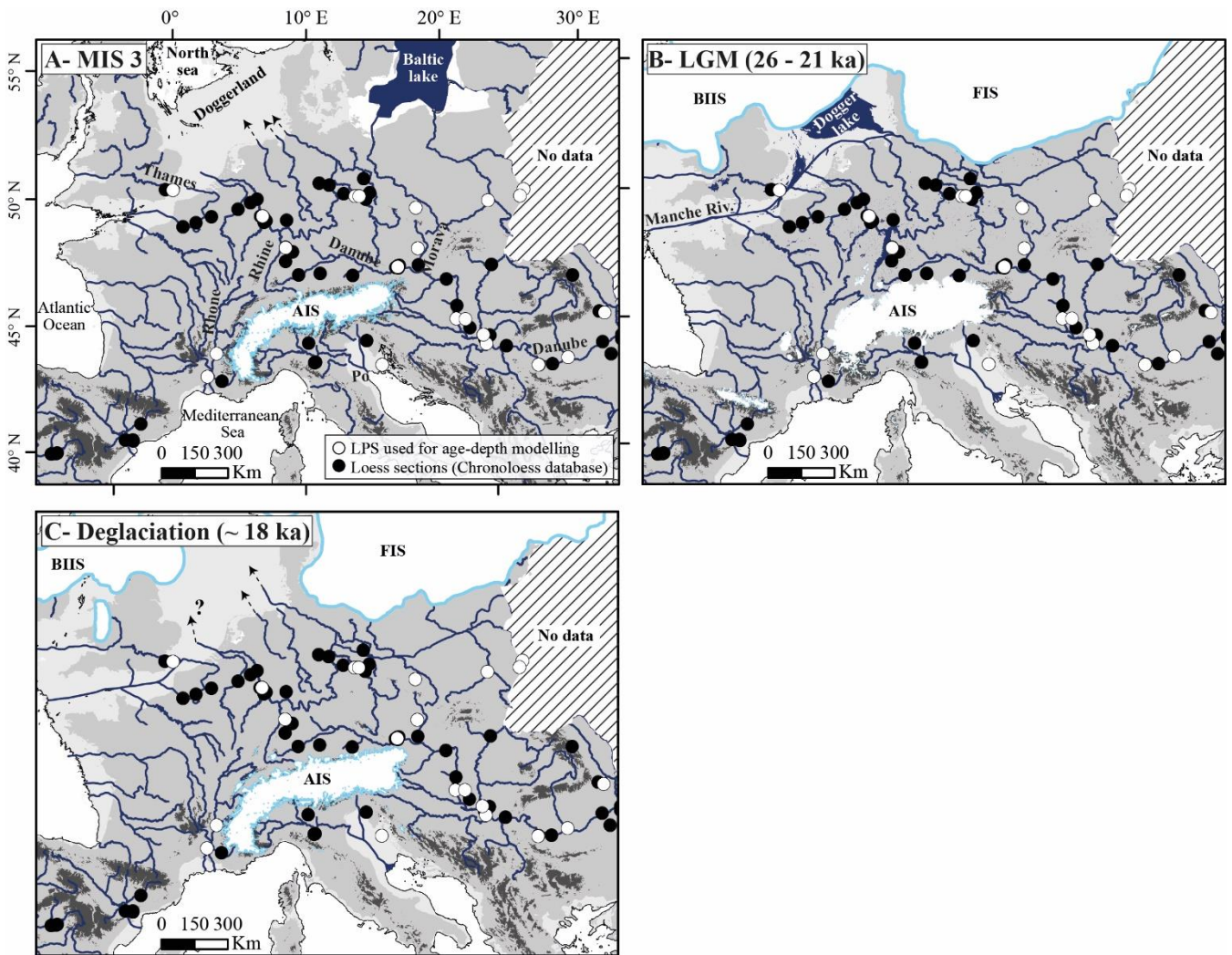
Figure 6: Palaeogeographic maps of Europe. A) 38-35 ka time slice (GI-8, GI-7); the Baltic lake is from (Lambeck et al., 2010). B) 26-21 ka time slice. (C) ca. 18 ka. The sea levels are from Lambeck et al. (2014).
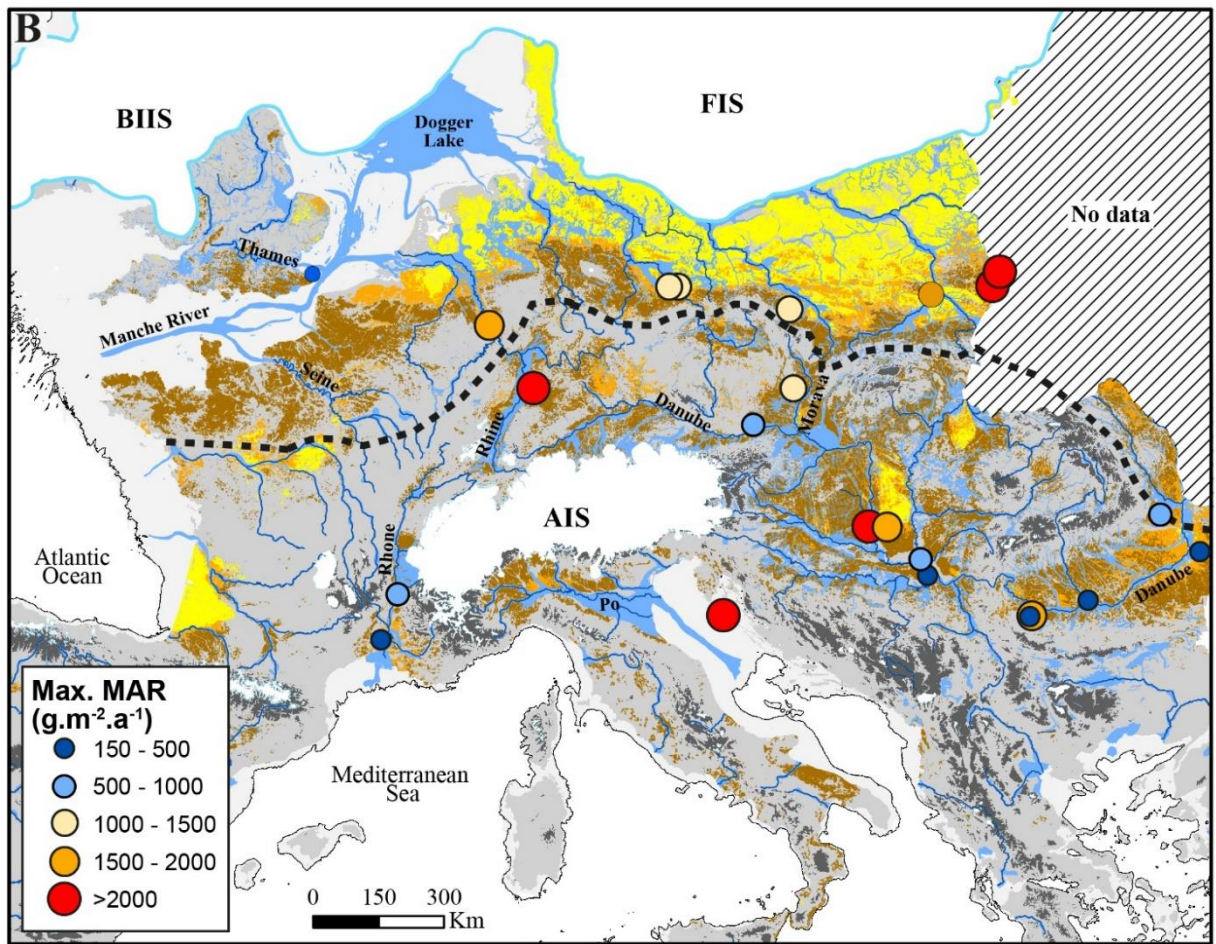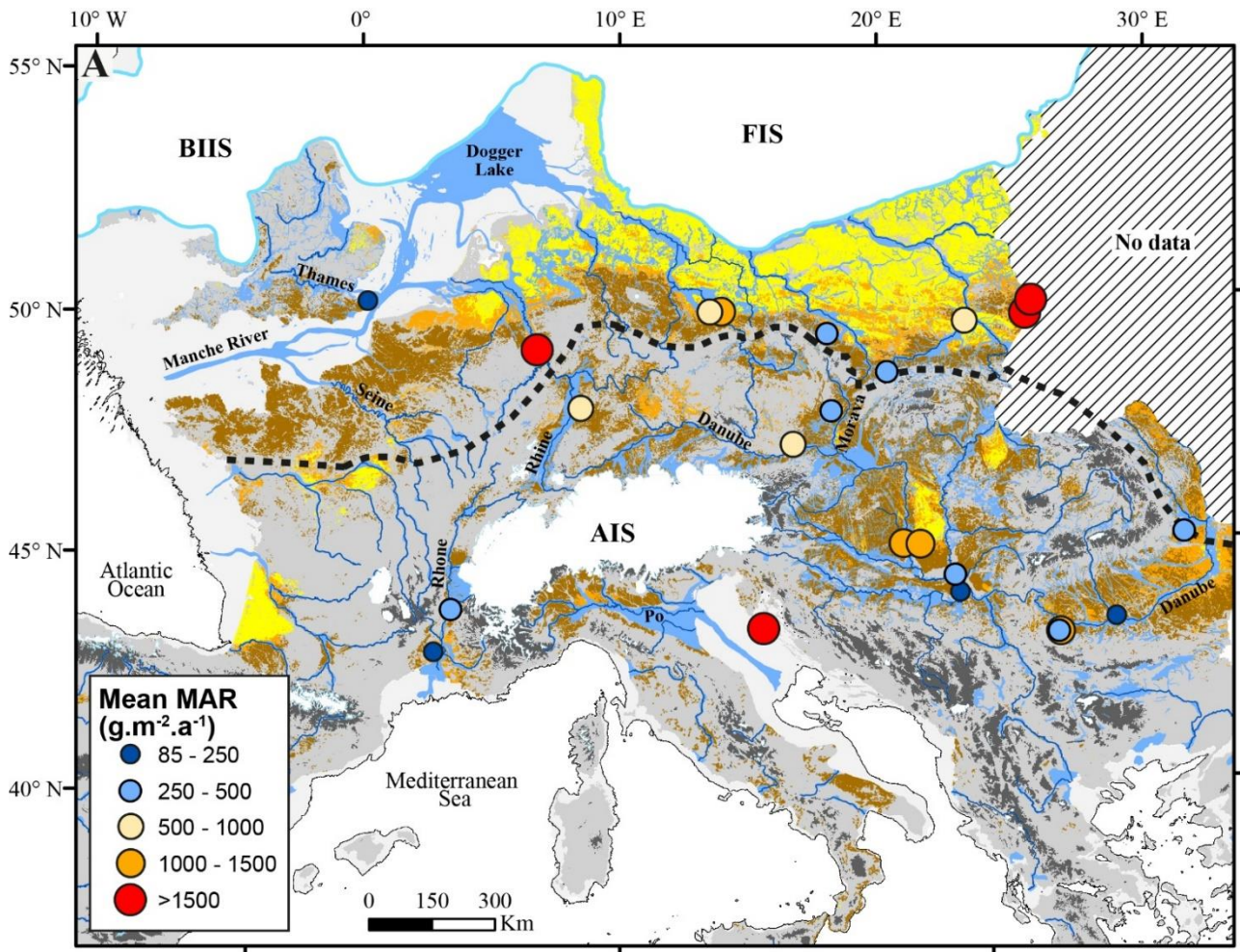
965 **Figure 7**: Mean (A) and maximum (B) MARs of European loess during the last 60 ka b2k.
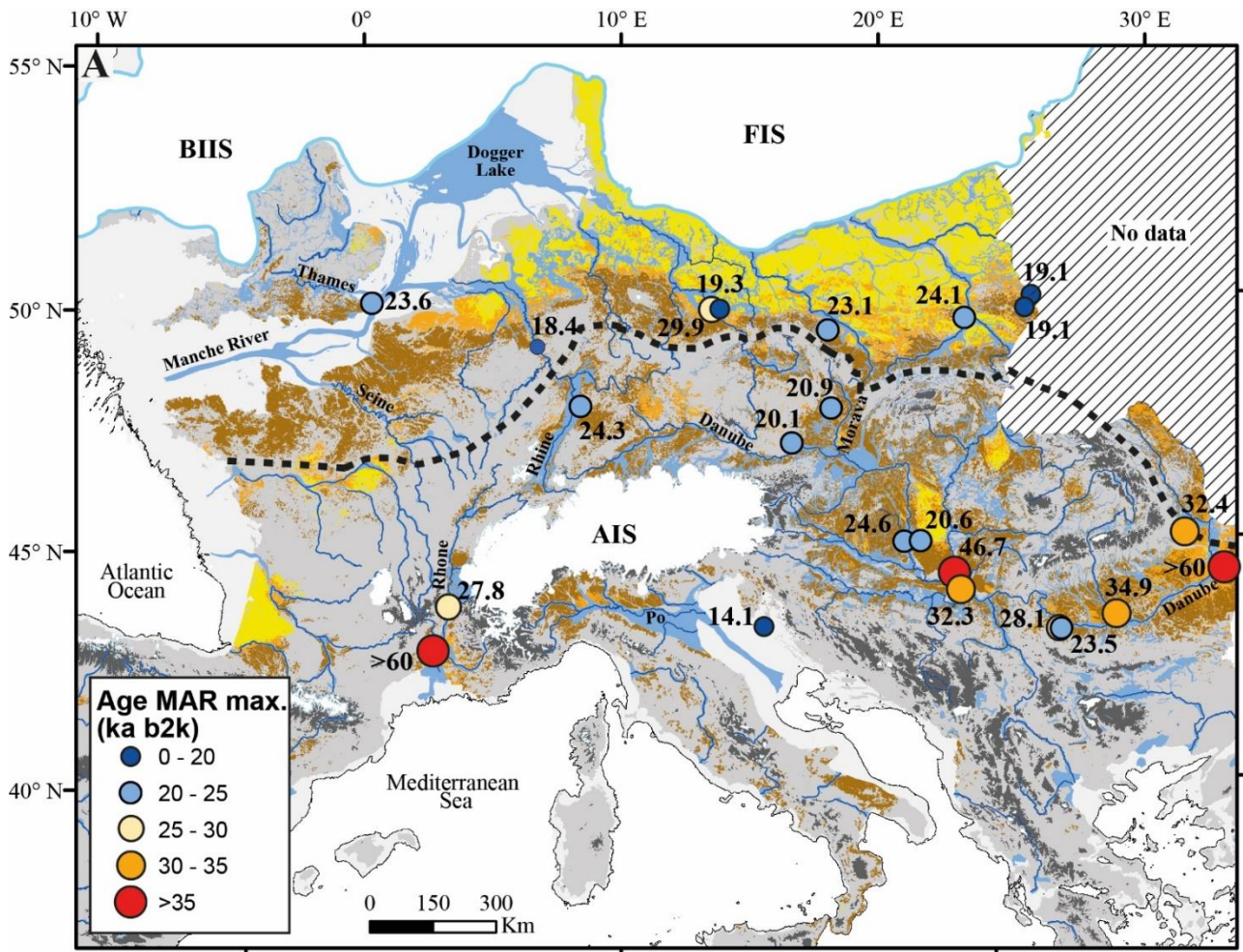
Figure 8: Age of the maximum MARs of European loess.